A competitive disinhibitory network for robust optic flow processing in *Drosophila*

Mert Erginkaya[1], Tomás Cruz[1], Margarida Brotas[1,2], Kathrin Steck[3], Aljoscha Nern[4], Filipa Torrão[1], Nélia Varela[1], Davi Bock[5], Michael Reiser[4] and M Eugenia Chiappe[1,6,*]

[1] *Champalimaud Neuroscience Programme, Champalimaud Centre for the Unknown, Lisbon, Portugal*

[2] *CEDOC, iNOVA4Health, NOVA Medical School, Universidade Nova de Lisboa, Lisbon, Portugal*

[3] *Center for Teacher Education and School Research, Universität Leipzig, Leipzig, Germany*

[4] *Janelia Research Campus, Howard Hughes Medical Institute, Ashburn, VA*

[5] *University of Vermont College of Medicine, VT*

[6] *Lead contact*

*Correspondence should be addressed to eugenia.chiappe@neuro.fchampalimaud.org

Summary

Many animals rely on optic flow for navigation, using differences in eye image velocity to detect deviations from their intended direction of travel. However, asymmetries in image velocity between the eyes are often overshadowed by strong, symmetric translational optic flow during navigation. Yet, the brain efficiently extracts these asymmetries for course control. While optic flow sensitive-neurons have been found in many animal species, far less is known about the postsynaptic circuits that support such robust optic flow processing. In the fly *Drosophila melanogaster*, a group of neurons called the horizontal system (HS) are involved in course control during highspeed translation. To understand how HS cells facilitate robust optic flow processing, we identified central networks that connect to HS cells using full brain electron microscopy datasets. These networks comprise three layers: convergent inputs from different, optic flow-sensitive cells, a middle layer with reciprocal, and lateral inhibitory interactions among different interneuron classes, and divergent output projecting to both the ventral nerve cord (equivalent to the vertebrate spinal cord), and to deeper regions of the fly

brain. By combining two-photon optical imaging to monitor free calcium dynamics, manipulating GABA receptors and modeling, we found that lateral disinhibition between brain hemispheres enhance the selectivity to rotational visual flow at the output layer of the network. Moreover, asymmetric manipulations of interneurons and their descending outputs induce drifts during highspeed walking, confirming their contribution to steering control. Together, these findings highlight the importance of competitive disinhibition as a critical circuit mechanism for robust processing of optic flow, which likely influences course control and heading perception, both critical functions supporting navigation.

Keywords

Optic flow, self-motion estimation, Drosophila, recurrent inhibition, steering control, heading perception, navigation

Introduction

As we navigate through space, our senses are continuously bombarded with a variety of stimuli from the environment and our own movements. Even for seemingly straightforward information, such as determining if we are veering to the left or right, our brains must extract and process the relevant signals from all incoming inputs to reorient according to our goals. Sensorimotor circuits that combine feedforward excitation with lateral inhibition have frequently been associated with this type of binary categorization[1,2] and behavioral choice[3–5]. However, the precise mechanisms by which sensory signals are transformed within these sensorimotor circuits are poorly understood.

Many animals rely on coherent patterns of image velocity across the retina to navigate according to goals. These patterns result from the relative motion between the moving observer and the surrounding scene, commonly known as optic flow[6,7]. The specific optic flow experienced by the observer depends on the direction and speed of the eyes, head, and

body. Therefore, optic flow provides valuable information about gaze, heading and traveling directions, allowing for a comparison with the intended trajectories for course control. Indeed, optic flow-sensitive neurons, which poses large monocular receptive fields sensitive to different axes of movement[8–11] are found across the animal kingdom[12–17] and have been implicated in heading perception, and gaze and course control[18–23]. Additionally, optic-flow sensitive neurons integrate multimodal information to distinguish between self-generated and externally generated information[13,24–27]. However, for accurate extraction of self-motion information, binocular integration between the eyes is also necessary. While some lateral interactions within optic flow-sensitive neurons have been identified[17,28–31], the precise mechanisms through which postsynaptic circuits integrate bilateral optic flow information to disambiguate self-motion and contribute to goal-directed navigation remain largely unknown.

The fly *Drosophila melanogaster* offers a valuable opportunity to investigate the circuit mechanisms involved in processing optic flow robustly. With its impressive visually guided behaviors, versatile genetic toolkit, comprehensive brain electron microscopy datasets, and well-characterized populations of optic flow-sensitive neurons, *Drosophila* allows for a systematic identification, and precise dissection of these mechanisms. In *Drosophila*, optic flow-sensitive neurons called lobula plate tangential cells (LPTCs) are found in deep layers of the fly's optic lobe and project to premotor regions of the brain. Certain LPTCs, like the horizontal system (HS) cells and H2 cells are sensitive to horizontal optic flow[32–34]. They receive non-visual signals related to angular velocity, which enhance their selectivity to the fly's rotations during spontaneous walking[27,33]. HS and H2 cells can also drive rotations of the fly[27,33,35], implicating them in course control. Recent work has shown that HS cells play a significant role in steering an exploratory fly, particularly during high-speed walking[35,36], when optic flow is dominated by symmetric translational components, which may overshadow the asymmetric ones caused by the fly's unexpected rotations. Thus, investigating HS cells and

their postsynaptic pathways provides an opportunity to understand how the network process optic flow robustly, even in situations with a low signal-to-noise ratio.

In this study, we conducted a systematic analysis of the structure and function of synaptic partners of HS and H2 at their central axon terminals. Our findings revealed that HS and H2 cells form a subnetwork comprising three layers, including an input layer of converging LPTCs, a middle layer of several classes of GABAergic interneurons, and divergent outputs projecting back to the lobula plate (feedback), to the ventral nerve cord (VNC, the insect analogous of the vertebrate spinal cord), or to deeper premotor regions of the fly brain. The inhibitory layer forms recurrent connections with LPTCs and provides lateral inhibition across the two brain hemispheres. Using two-photon calcium imaging of the newly identified interneurons along with manipulating GABA receptors and modeling, we found that a lateral disinhibition motif enhances rotational sensitivity at the network's output layer, supporting steering control in freely exploring flies. Overall, our study unveils the layered anatomical structure of optic flow networks and their strong modulation by inhibitory feedback and elucidates how feedforward excitation combined with lateral disinhibition enables robust extraction of asymmetries in optic flow signals between the eyes to guide reorientation of a roaming fly.

Results

A class of optic flow-sensitive descending neuron contributes to steering during high-speed walking

Course deviations can be determined by analyzing the differences in the pattern of optic flow between the fly's eyes using binocular integration. However, these differences vary with the fly's walking speed. Even when the deviation from a straight course is the same, flies moving at low versus high speed induce distinct optic flow patterns (**Fig. 1a**, colored rectangles). At low walking speeds, asymmetries in the optic flow can be easily detected, but

102 at high speed, these asymmetries are largely reduced due to the prominent translational
103 components in the optic flow (**Fig. 1a**). We currently lack a complete understanding of how
104 the networks responsible for processing rotational optic flow estimate asymmetries that
105 remain consistent regardless of the fly speed, enabling reliable walking control.

106 The horizontal system cells (HS cells), whose receptive fields are predominately
107 monocular[32], play a role in steering, especially during high-speed walking[35,36]. Recent work
108 has shown that these cells interact laterally (across hemispheres) via gap junction coupling
109 through an unidentified interneuron[30], potentially improving the detection of asymmetric optic
110 flow. If these lateral interactions enhanced the detection of asymmetric optic flow, output
111 neurons from the HS network should display increased sensitivity to rotational optic flow and
112 binocular activity compared to HS cells.

113 To explore this idea, we compared the response properties of the descending neuron
114 DNp15[30,37] to those of their input HS cells concerning optic flow (**Fig. 1b,c**). We conducted *in*
115 *vivo*, 2-photon calcium imaging in immobilized flies within the inferior posterior slope (IPS)
116 region of the fly brain (**Fig. 1c,** see **Methods**) while presenting binocular asymmetric
117 horizontal motion (i.e., stimuli representing rotations along the yaw axis) or binocular
118 symmetric horizontal motion (i.e., stimuli representing translational-like movement along the
119 forward direction (**Supplementary Video 1,** "Front-to-back/Back-to-front" and "Yaw left/right"
120 stimuli, respectively). In addition, to identify binocular interactions, we compare the binocular
121 responses of HS and DNp15 cells to those induce by monocular stimuli.

122 We found that DNp15 exhibited response profiles and velocity tuning to binocular
123 asymmetric optic flow like HS cells, likely due to their electrical coupling[37] (**Fig. 1-S1a-c,**
124 **Supplementary Video 2**). However, DNp15 activity was more influenced by binocular
125 interactions compared to HS cells and showed a small but detectable response to
126 contralateral back-to-front visual motion (**Fig. 1d, 1-S1c**), suggesting an increased selectivity
127 to rotational optic flow. To describe the relative selectivity of HS and DNp15 to rotatonal vs.

128 translational stimuli, we defined a qualitative parameter called the discrimination index, which
129 compares the magnitude of the responses of a cell to rotational vs translational stimuli (see
130 **Methods**, **Fig. 1-S1e**). Overall, DNp15 demonstrated enhanced selectivity to rotational stimuli
131 than translational-like stimuli, unlike HS cells (**Fig. 1d,e, 1-S1d,e**). Thus, the network
132 associated with HS cells seems well suited to robustly detect asymmetries in binocular optic
133 flow for course control.

134 To test this idea, we investigated the role of DNp15 in walking control. DNp15 is
135 thought to contribute to gaze stabilization[37,38] and directly projects to dorsal neuropiles within
136 the tectulum of the ventral nerve cord[39] (VNC, the insect analogous of the spinal cord). Gaze
137 control depends on head-body coordination and course control[38]. Thus, we directly tested the
138 impact of DNp15 silencing on steering (course control) during highspeed walking by
139 expressing the inward rectifying potassium channel Kir2.1 in different configurations and
140 observing the walking paths of exploratory flies[38]. We created flies with unperturbed activity
141 of DNp15 (controls, i.e., no expression of Kir2.1), with balanced silenced DNp15 (bilateral
142 expression of Kir2.1), and with asymmetry in the activity of DNp15 (unilateral expression of
143 Kir2.1) (**Fig. 1-S1f**, see **Methods**). Flies typically exhibit runs of high forward velocity or turns
144 of low forward velocity (body saccades) under these experimental conditions (**Fig. 1f**, see also
145 **Fig. 6a**). We evaluated course control by calculating path deviation per run bout, or by
146 examining any biases during body saccades (**Fig. 1f,g**, **Fig. 1-S1g**, see **Methods**). Flies with
147 both DNp15 silenced or with no silencing did not show any bias during body saccades or runs
148 (**Fig. 1f,g** and **Fig. 1-S1g**, none or both silenced DNp15). However, unilateral silencing of
149 DNp15 resulted in contralateral path deviation during runs (**Fig. 1f,g**), while no biases were
150 observed during body saccades (**Fig. 1-S1g**, left or right silenced DNp15). These findings
151 suggest that asymmetry in activity of left vs. right DNp15 leads to steering biases during
152 forward walking. Furthermore, the enhanced selectivity of DNp15 to rotational vs. translational
153 optic flow implies that these neurons could detect minor differences in optic flow across the

154 eyes, thereby contributing to steering at high forward speed. However, the specific circuits
155 and mechanisms responsible for conveying such selectivity supporting robust optic flow
156 processing in DNp15 remain unknown.

157 **HS, H2 and VS cells connect distinctively to two parallel central networks**

158 To uncover the circuit and mechanisms responsible for robust rotational optic flow
159 processing, we investigated the downstream central synaptic partners of well-characterized
160 rotational optic flow sensitive cells, such as HS, H2, and VS cells. We used a complete female
161 adult fly brain (FAFB) electron microscopy (EM) dataset[40] (**Fig. 1-S2a-b**, see **Methods**) to
162 map the location of chemical synapses at the axon terminals of these LPTCs. By manually
163 tracing and identifying pre and postsynaptic partners (**Fig. 1-S2c**, see **Methods** for tracing
164 strategy), we found that HS, H2 and VS cells establish both input and output synaptic sites,
165 revealing central modulation of axonal activity in HS, H2 and VS cells (**Fig. 1-S2c-d**). We also
166 observed that these cells form few strong connections and numerous weak connections with
167 their synaptic inputs and outputs (**Fig. 1-S3a,b**). These results were confirmed using two
168 additional EM datasets with semi-automatically reconstructed neurons, FlyWire[41] and
169 Hemibrain[42] (**Fig. 1-S2a,c,d, S3**, **Supplementary Table 1**). Hence, our manual tracing
170 approach effectively identified important synaptic partners of HS, VS, and H2 cells. We
171 defined neurons providing more than 10 synaptic inputs to or receiving more than 35 synaptic
172 outputs from LPTCs as strong synaptic partners (**Fig. 1-S2d**, black lines).

173 To analyze the central networks involving these LPTCs, we computed a connectivity
174 matrix among all identified strong partners in the FAFB dataset (**Fig**. **2-S1**, see **Methods**).
175 While the matrix displayed rather sparse connections with weak or no connections between
176 most neuron pairs, certain pairs exhibited strong unidirectional connections with hundreds of
177 synapses (**Fig. 2-S1**). We performed a hierarchical cluster analysis on the pairwise number
178 of synapses (**Fig. 2-S1**, see **Methods**), and identified three primary clusters: HS and VS cells

179 with the interneuron IVLPT8, and two clusters forming separate networks with HS and VS
180 cells (**Fig. 2-S1** and **2a**). Importantly, this network structure remains mostly unchanged by
181 thresholding (**Fig. 2-S2**).

182 The VS network demonstrated strong connections between VS and central
183 interneurons (**Fig. 2a**), with output pathways diverging into descending pathways, including
184 neck motor neurons, and descending neurons (DNs), and feedback pathways to the ocelli,
185 the secondary optical system of flies[43,44]. On the other hand, the H2-HS network exhibited
186 strong connections among central interneurons, H2 and HS cells, and the GABAergic
187 feedback CH cells[45,46] (**Fig. 2a**). Like the VS network, the outputs of the HS-H2 network
188 diverged, with a descending pathway defined by several DNs projecting to leg, neck, and
189 haltere neuropiles in the VNC[39,47], and an ascending pathway of interneurons projecting to the
190 lateral accessory lobes (LAL).

191 The VS connections represented only a small proportion of total connections within
192 the H2-HS network and vice versa (**Fig. 2b**). This suggests that both networks largely operate
193 independently from each other. Notably, the DNs of the HS-H2 network are different from
194 those of the VS network, pointing towards parallel operation. Two DN outputs of the HS-H2
195 network, DNa02 and DNp15 have been previously characterized (**Fig. 1**)[37,47]. These neurons
196 are sensitive to fly rotations (or their visual consequence) and contribute to steering. The LAL,
197 the other output region of the HS-H2 network, is a higher-order premotor area of the insect
198 brain, thought to contribute to steering[48,49]. Together, these findings strongly support the
199 involvement the HS-H2 network in steering control.

200 **Recurrent connections define the intermediate layer structure of both networks**

201 The two networks, though largely non-overlapping, converge at the level of LPTC cells,
202 connecting to a small set of interneurons within the intermediate layers of the networks (i.e.,
203 between LPTCs and their outputs). We identified five distinct classes of LPTC input cells within

204 these intermediate layers that provide specific, recurrent input to HS, H2 and VS cells, thereby
205 defining the structure of the two networks (**Fig. 2-S3a-c**). Three of the five classes are
206 collectively defined as lobula plate tangential cell recurrent neurons (LPTCrns), due to their
207 shared soma location and tract, indicative of a common developmental origin. We differentiate
208 them based on anatomical features (**Fig. 2-S3b-d**).

209 Crab LPTCrn cells (**cLPTCrn**), central components of the VS network (**Fig. 2b**), extend
210 prominent projections to both hemispheres of the PS and connect reciprocally with most VS
211 and HS cells (**Fig. 2c**). Bilateral LPTCrn cells (bLPTCrn) also project to both hemispheres of
212 the PS, but their contralateral projections are limited to the dorsal area of the PS (**Fig. 2-S3b**).
213 Unilateral LPTCrn cells (uLPTCrn) are prominent components of the H2-HS network (**Fig. 2b**).
214 They project to the ipsilateral side and exhibit strong reciprocal connections with HS, H2, and
215 VS1-2, and VS7,8 cells (**Fig. 2c**).

216 The remaining two LPTC input classes specifically connect to HS and H2 cells. The
217 first class involves bilateral inferior posterior slope neurons (bIPS, **Fig 2-S3b**), which receive
218 strong convergent projections from ipsilateral HS and contralateral H2 cells and send
219 projections to the contralateral HSN and HSE cells (**Fig. 2c**). Notably, the two contralateral
220 CH cells are the strongest downstream partners of bIPS, receiving over 450 synapses from
221 bIPS as their strongest input (**Fig. 2-S1**). This provides strong anatomical evidence for a
222 central feedback pathway within this network. The second class of interneurons selectively
223 connects to the contralateral H2 cells at their axon terminals (**Fig. 2c**), referred as H2 recurrent
224 neurons (H2rn) as they receive input back from contralateral H2 cells.

225 The primary brain regions that send information to the intermediate layers of the VS
226 and HS-H2 are the PS, gnathal ganglion (GNG), and optic lobes. Additionally, all five cell
227 types receive direct ascending input from the VNC (**Fig. 2-S3e, Fig. 3b**). Thus, the
228 intermediate layers may operate as both integrators and broadcasters: they likely integrate
229 multimodal signals to modulate the optic flow sensitive networks, and broadcast optic flow

230 signals to numerous regions of the fly's CNS. The recurrent connections between LPTCs and
231 different classes of LPTC input neurons in the central brain suggest that these interneurons
232 possess distinct optic flow sensitivities based on their LPTC inputs, integrate extraretinal
233 signals in addition to optic flow, broadcast modulatory signals from premotor centers, and
234 shape the optic flow sensitivity of output neurons. Different sets of central interneurons within
235 the intermediate layers of the two networks may contribute in different visual-motor contexts.
236 In the following sessions, we focus on the functional properties of neurons within the different
237 layers of the HS-H2 network, and how optic flow signals are transformed to enhance DNp15's
238 selectivity to horizontal optic flow compared to HS cells.

239 **The H2-HS network exhibit responses to optic flow that are not entirely predicted by**
240 **their LPTC inputs**

241 To understand how the enhanced selectivity to rotational optic flow in DNp15 emerges
242 from the structure of the HS-H2 network, we characterized the optic flow responses of the
243 intermediate layer of the H2-HS network, which connect to DNp15 (**Fig. 2-S3f, Fig. 3a**). To
244 achieve cell-type-specific genetic access, we used traced EM skeletons to identify neurons in
245 transgenic line libraries (see **Methods, Fig. 3-S1a**). In vivo, neural recordings were conducted
246 under non-behaving conditions, focusing specifically on optic flow processing while minimizing
247 the potential impact of non-visual signals present in both LPTCs[25,27,33,50,51] and the network's
248 interneurons (**Fig. 3b**). We characterized neural responses to various patterns of optic flow
249 (**Supplementary Video 1**) by measuring calcium dynamics at axon terminals (e.g., **Fig. 3c**,
250 see **Methods** for choice of calcium indicators).

251 bIPS, uLPTCrn, and H2rn cells displayed responses to horizontal optic flow and
252 velocity tuning that showed similarities and differences compared to their inputs HS and H2
253 cells, (**Fig. 3d, Fig. 3-S2, Supplementary Video 2)**. First, uLPTCrn cells, which receive direct
254 input from VS (**Fig. 2c**), exhibited minimal or negative calcium signals to pitch and roll optic

255 flow, which would be expected to excite their presynaptic inputs from VS cells (**Fig. 3-S2a**).
256 Second, each class of interneurons displayed characteristic velocity tuning. While uLPTCrns
257 are more sensitive to slower than faster speeds, bIPS exhibit larger responses to intermediate
258 speeds, and H2rns are more sensitive to faster than slower speeds, in contrast to their
259 presynaptic H2 cells. These results suggest that cell autonomous properties or additional
260 inputs to these interneurons modulate visual responses of uLPTCrns and H2rns, either
261 through direct connections from other optic lobe neurons, or indirectly through inputs from the
262 central brain (**Fig. 3b**).

263 Further evidence for network-based modulation of visual inputs came from the
264 analysis of the responses of interneurons to monocular stimuli. bIPS and uLPTCrn cells
265 receive converging inputs from ipsilateral HS and contralateral H2 neurons (**Fig. 3a**), which
266 respond to progressive (front-to-back) and regressive (back-to-front) monocular motion,
267 respectively (**Fig. 3-S2c**). Accordingly, one would expect both cell types to respond to
268 ipsilateral progressive and contralateral regressive stimuli. However, while both cell types
269 responded to progressive stimuli, they showed minimal responses to contralateral regressive
270 motion (**Fig. 3-S2c**), unlike their H2 inputs. Conversely, H2rn cells responded to contralateral
271 regressive motion, as excepted from their inputs from H2 cells, but they also responded to
272 progressive motion (**Fig. 3-S2c**) despite not receiving direct input from HS cells. Thus,
273 additional inputs from the central brain likely convey visual information indirectly to H2rn cells.
274 Nevertheless, responses to binocular asymmetric stimuli were larger than monocular
275 horizontal motion in all cells (**Fig. 3d-e**), suggesting binocular interactions at the intermediate
276 layer. Together, these findings demonstrate that the sensitivity to optic flow in different classes
277 of interneurons within the H2-HS network are modulated by network activity and their central
278 inputs, with strong binocular interactions. Specifically, both uLPTCrns and bIPS display
279 binocular optic flow selectivity that cannot be entirely explained by their direct H2 inputs.

280 **Neurons within the H2-HS network show distinctive optic flow selectivity**

281 The lack of responses to contralateral regressive motion in bIPS and uLPTCrn
282 suggests that these interneurons might be equally sensitive to translational and rotational
283 optic flow. To test this idea, we examined their responses to binocular symmetric and
284 asymmetric stimuli (**Fig. 3-S2d**). We presented binocular translational motion or binocular
285 symmetrical horizontal motion (translation-like stimulus). The former stimuli contain
286 progressive or regressive horizontal components combined with vertical downward or upward
287 components, respectively, to mimic the visual consequence of the body's forward or backward
288 translation. The latter stimuli contain only horizontal progressive or regressive components,
289 representing what a horizontal-selective system may respond to in the context of translation
290 (**Supplementary Video 1,** "Progressive/regressive" and "Front-to-back/Back-to-front",
291 respectively). The three interneurons exhibited characteristic response profiles to these stimuli
292 (**Fig. 3d,e Fig. 3-S2d**). bIPS was most active with binocular symmetric horizontal stimuli
293 compared to translational progressive stimuli (**Fig. 3d,e**). uLPTCrn cells showed minimal or
294 negative responses to translational patterns, while H2rns showed positive response to both
295 regardless of the direction of motion, albeit weakly (**Fig. 3d,e, 3-S2d**).

296 To describe the relative selectivity of HS, H2, bIPS, uLPTCrns, and H2rns to rotational
297 vs. translational stimuli by calculating the discrimination index (see **Methods**, **Fig. 1-S1e**, **3f**).
298 HS and H2 responded to both rotational and translational optic flow. However, they were
299 relatively, albeit weakly, more selective to rotational optic flow, resulting in a slightly negative
300 discrimination index closer to zero compared to uLPTCrn and H2rn cells, which showed
301 enhanced selectivity for rotational optic flow, particularly when compared to the more
302 naturalistic translational optic flow. bIPS also responded to both rotational and translational
303 patterns in a selective manner; however, bIPS exhibited a relatively stronger sensitivity to
304 binocular horizontal symmetric stimuli and thus have a discrimination index skewed more
305 towards translations compared to rest of the H2-HS network cells (**Fig. 3f**).

306 We expanded our translational optic flow characterization (**Fig. 3-S3a**,
307 **Supplementary Video 1**) and observed that bIPS, like HS and H2 cells, exhibited its strongest
308 translational sensitivity to compound optic flow-fields, with sideslip and forward components
309 (**Fig. 3-S3b-d**). However, translational patterns with backwards motion which elicited activity
310 in H2 cells (**Fig. 3-S3c**) have minimal impact on bIPS. H2rns and uLPTCrns on the other hand,
311 minimally increased or decreased their activity during forward and backward translations (**Fig.**
312 **3-S3e-f**), becoming mostly sensitive to changes in sideslip translations (**Fig. 3-S3g**). Taken
313 together, these results demonstrate that neurons downstream of HS and H2 cells have
314 increased selectivities to characteristic patterns of optic flow. The question remains as to how
315 a neuron like bIPS, which is embedded in a rotational-sensitive network, enhances its
316 selectivity for translational or translational-like optic flow patterns, and what function this
317 response property provides to the network.

318 **Inhibitory interactions fine tune optic flow sensitivity in bIPS**

319 We hypothesized that the lack of responses to contralateral regressive motion in bIPS,
320 and its enhanced selectivity to translational optic flow could arise from recurrent interactions
321 between excitatory LPTCs and inhibitory interneurons. For example, excitation provided by
322 H2 to bIPS could be suppressed by indirect, H2-dependent inhibition. To identify possible
323 candidates, we analyzed the predicted neurotransmitter[52] for bIPS input neurons (**Fig. 4a**).
324 The two main inputs to bIPS are uLPTCrn and H2rn, both of which are GABAergic (**Fig. 4-S1**)
325 and receive prominent inputs from H2 (**Fig. 4b**). The subcellular organization of H2, HS,
326 uLPTCrn and H2rn inputs relative to the root point of bIPS (**Fig. 4-S2a**) suggests that these
327 neurons tend to make synapses closer to the root point than other bIPS inputs (**Fig. 4-S2b-**
328 **c**). H2rn synaptic inputs onto bIPS tend to be closer to H2 inputs than HS inputs (**Fig. 4-S2d**),
329 often forming microcircuit motifs with H2 (**Fig. 4-S2e, g**) but not with HS cells (**Fig. 4-S2f, h**).
330 Thus, this local connectivity structure could suppress H2-related excitation through H2rns, but

331 it may not fully account for the lack of responses to contralateral regressive motion in bIPS
332 (**Fig. 3-S2c**). Another possibility is that both H2rns and uLPTCrns contribute to this
333 suppression.

334 To test this idea, we perturbed fast-acting GABA signaling in bIPS using the FlpStop
335 genetic strategy[53]. We targeted the Resistance to dieldrin (Rdl) gene[54] since it is essential for
336 functional $GABA_A$ receptors[55,56] (GABAARs). Overall, bIPS' responses to optic flow Rdl-
337 FlpStop flies were decreased relative to control flies (**Fig. 4c-e**), including lack of negative
338 calcium responses to non-preferred directions of stimulus motion (**Fig. 4c-d**). Notably, the
339 effect of disrupting $GABA_A$ signaling was most evident for translational and translational-like
340 optic flow (**Fig. 4c-e**). This caused the discrimination index between translational-like and
341 rotational optic flow responses to skew towards zero (i.e., equal discriminability), while the
342 discrimination index between translation and rotational optic flow remained unaffected (**Fig.
343 4f**). These results suggest that the enhanced selectivity to horizontal binocular symmetric
344 motion, as well as the responses to the non-preferred directions of motion are mediated by
345 GABAARs in bIPS. However, contralateral regressive responses that drive H2 activity remain
346 unaffected under Rdl-FlpStop (**Fig. 4c**, "left CW"), indicating that signals from H2 are gated
347 by other mechanisms. Taken together, these findings show that GABAergic inhibition
348 modulates bIPS' selectivity to binocular symmetric optic flow within the network. We propose
349 that this selectivity may play a key role in enhancing the asymmetries in the activity of left
350 versus right postsynaptic partners, particularly in the sensory context of translational optic flow
351 where the visual input becomes more symmetric (**Fig. 1**).

352 **Reciprocal inhibitory connections in the middle layer of the H2-HS network promote
353 competition between the left and right sides for steering control**

354 Our Rdl-FlpStop experiments suggest that inhibitory input onto bIPS enhances its
355 responses to binocular symmetric stimuli. Because bIPS is an inhibitory neuron, its selectivity

356 may facilitate the detection of minor binocular asymmetries at the output layer of the network.
357 However, bIPS is embedded in a reciprocal motif with contralateral uLPTCrns (**Fig. 3a**),
358 making it challenging to understand the role of this motif in a dynamic setting like locomotion.
359 Therefore we implemented a phenomenological model agent[33] constrained by the connectivity
360 structure of the HS-H2 network (**Fig. 5, 5-S1**, see **Methods**), to study the role of bIPS and
361 uLPTCrns on steering control. Our agent processes horizontal motion to guide steering of a
362 virtual fly, like an exploratory real fly[38]. We built a model with four input channels, each
363 containing classical visual motion detectors[28], and the core cross-inhibitory circuit architecture
364 of the H2-HS network (**Fig. 5a**). The model was tuned to match the real neural data for
365 horizontal motion stimuli (see **Methods**, **Fig. 5-S1a-c** and **5b**).

366 We tested the effect of removing the inhibitory input to bIPS in the model by removing
367 ipsilateral uLPTCrns inputs. This manipulation abolished the enhanced responses of bIPS to
368 binocular symmetric stimuli (**Fig. 5c**) and affected the discriminability of the modeled cell to
369 rotational vs translational-like stimuli, like in the real fly (**Fig. 5d**). Based on these results, we
370 concluded that this simplified core model architecture, combining direct excitation with lateral
371 disinhibition, can replicate the visual responses of the input and middle layers of the H2-HS
372 subnetwork.

373 Next, we tested the contribution of the lateral inhibition provided by bIPS to the output
374 responses of the network in the context of course control. This agent fly compares the activity
375 of a left and right pair of DNs, akin DNp15, to impose steering control (**Fig. 5e**). Removing
376 bIPS from the model reduced the asymmetry between left and right DNp15 cells, leading to a
377 reduced ability to discriminate asymmetries in binocular horizontal motion during translations
378 at high speed (**Fig. 5f**). Removing both uLPTCrns and bIPS further reduced the asymmetry
379 between left and right DNp15 activity down to the level of HS. Like DNp15, activity of uLPTCrn
380 cells across the two eyes also became more symmetric upon removing bIPS (**Fig. 5f**).
381 Conversely, removing uLPTCrn cells made bIPS less sensitive to horizontal symmetric

binocular motion (**Fig. 5c**). Thus, the reciprocal inhibitory and lateral interactions within the middle layer of the H2-HS network support enhanced sensitivity to differences between the eyes at the output layer in the context of translations. Indeed, the asymmetry in DNp15 and uLPTCrn cells remained high in ranges of forward velocities typically observed in exploratory flies, and we propose that this is aided by the increased symmetric activity in bIPS as a function of translation speed (**Fig. 5g**).

To test the direct contribution of bIPS to steering in the context of highspeed translation, we allowed our agent fly to freely explore a virtual arena where the fly's trajectory was determined by bouts of straight walking (forward runs) and rapid turns (saccades) away from the walls, similar to real flies exploring a comparable environment (**Fig. 6a, 5-S1d,** see **Methods**). As expected by model design, 'silencing' individual DNp15 cells predicted the angular bias observed in real flies under individual DNp15 silencing (**Fig. 6b,** see also **Fig. 1i**). Silencing individual bIPS neurons in the model induced biases during forward runs and performing the similar perturbation in real flies lead to similar results (**Fig. 6c, 6-S1a**). This finding demonstrated that asymmetries between left and right bIPS activity, consistent with the neuron's translational optic flow selectivity (**Fig. 3-S3**), are sufficient to bias the course direction of walking flies (**Fig. 6c**). Consistent with the model, bilateral manipulations of activity of bIPS did not affect the course of forward runs of real flies (**Fig. 6d**).

In summary, our findings support the idea of a central multilayer network that monitors rotational components of optic flow during translation and that amplifies asymmetric activity between right- vs. left outputs by lateral, competitive disinhibition, thereby increasing the rotational signal even in the context of prominent translational optic flow (**Fig. 6e**). This reciprocal, lateral inhibition therefore supports robust optic flow processing and increases the performance of networks contributing to course control, two functions that are especially important while walking at high speed.

407 ## Discussion

408 In this study we investigated how visuomotor circuits discriminate sensory signals in
409 challenging circumstances imposed by an animal's own locomotion. Through a combination
410 of full-brain EM reconstruction, modeling, optical imaging and behavior experiments, we
411 discovered a multi-layer network in the *Drosophila* central brain responsible for robust optic
412 flow processing and steering of exploring flies based. The first layer consists of optic flow
413 sensitive visual projection neurons, which form two networks with distinct sets of interneurons
414 and outputs. Both networks exhibit specific and recurrent connections between LPTCs and a
415 set of GABAergic inhibitory interneurons. Furthermore, there are critical reciprocal and lateral
416 interactions among the middle layer and across the hemispheres. The output layers receive
417 direct and indirect connections from the input layer, with the indirect pathway strongly
418 influenced by lateral disinhibition of the middle layer. This configuration allows the output
419 layer to generate a robust estimate of the fly's rotations, as indicated by their visual
420 consequence. Our findings unveils a network motif of competitive disinhibition[4] that enhances
421 the detection of asymmetries in optic flow across the eyes, enabling course control even in
422 the presence of highly symmetric bilateral visual motion cues (**Fig. 6e**).

423 **Parallel networks process visual feedback in the fly brain**

424 Until now, the few identified neck motor and descending outputs of HS and VS cells
425 have been shown to connect to either HS or VS cells[30,37,57,58] (CNMN6[59] being the single
426 exception). As such, HS and VS cells have been proposed to contribute to movement control
427 through largely parallel pathways. However, if downstream circuits of these LPTCs do not
428 converge, how can flies accurately estimate their self-movement when their natural
429 maneuvers during locomotion involve multiple axes of rotation and translation? By identifying
430 the major synaptic partners of HS, H2 and VS cells in the central brain (**Fig. 2**) we have found
431 that these LPTCs operate largely in parallel, connecting to distinct sets of descending, neck

432 motor and central brain output neurons. However, HS, H2 and VS cells also converge onto
433 anatomically distinct classes of GABAergic interneurons in the posterior slope. These
434 interneurons recurrently connect to different and complementary combinations of HS, H2 and
435 VS, suggesting the integration of orthogonal axes of optic flow at the central brain (**Fig. 3**).
436 We propose that this partially overlapping recurrent motif enables accurate processing of
437 naturalistic optic flow, modulating the concerted activity of LPTCs based on distinct visuomotor
438 conditions, and other internal contexts. Indeed, the identified inhibitory classes receive inputs
439 from motor and premotor areas of the fly CNS, including the VNC, PS, and GNG (**Fig. 2-S3**).
440 This feedback structure indicates strong processing of multimodal signals to differentially
441 modulate the activity of LPTCs and their postsynaptic outputs. These outputs likely contribute
442 to different motor programs and higher-order functions. For example, outputs of the H2-HS
443 network such as DNa02[47], DNp15[30,37] and VCNMN[57,60,61] have all been proposed to control
444 rotations of the body and the head along the yaw axis, while outputs of the VS subnetwork
445 such as DNp20 and ocelli have been implicated in gaze stabilization control along the roll
446 axis[60,62,63]. Each network project to neck-, leg-, and haltere-related regions in the VNC,
447 implicating LPTCs in the control of head and body movement independently but likely within
448 the context of head-body coordinated (gaze) motor programs occurring during exploratory
449 walking[38,64] and flight[65]. Additionally, output pathways that bridge LPTC activity with higher-
450 order brain regions, such as lateral accessory lobe and central complex via PS047, can
451 provide accurate internal self-motion estimates for heading perception and path integration
452 during navigation[66–69].

453 **GABAergic inhibition modulates asymmetries in visual motion processing**

454 Three cell types in the intermediate layers of H2-HS subnetwork, namely bIPS,
455 uLPTCrn and H2rn cells, exhibit optic flow sensitivities that are only partially explained by their
456 upstream LPTCs. This finding indicates that additional inputs influence their optic flow

457 sensitivity (**Fig. 3**). We have identified one group of such inputs: reciprocal connections among
458 the three cell types. These connections play a critical role in transforming optic flow signals
459 within the middle layer. For example, when fast acting GABAergic inputs to bIPS are
460 disrupted, the negative response caused by non-preferred directions of optic flow is eliminated
461 (**Fig. 4**). This effect is similar to the modulation of non-preferred visual motion responses in
462 the fly early visual system[70,71]. Furthermore, the same perturbation reduces bIPS' selectivity
463 to symmetric horizontal optic flow. Our constrained model suggests that this reduction is
464 partially caused by the inhibitory population of uLPTCrns, thereby likely affecting the
465 enhanced sensitivity to rotational optic flow by the output of the network. However, and
466 contrary to the expectations based by the connectivity structure, rapid GABAergic inputs do
467 not influence bIPS's responses to regressive, back-to-front optic flow. Although bIPS receive
468 strong connections from H2, signals from these synapses are not transmitted under non-
469 behaving conditions. One possibility is that the GABAergic population of H2rns controls this
470 signaling through other GABA receptors in bIPS. Alternatively, the gating of regressive signals
471 from H2 may involve other mechanisms, including neuromodulation. Further investigation will
472 explore the conditions under which bIPS respond to regressive information, which may render
473 the neuron more sensitive to asymmetric optic flow stimuli. Nevertheless, this finding
474 highlights the importance of combining EM connectivity with physiology to uncover context-
475 dependent modulation of brain circuits.

476 **Reciprocal inhibition in optic flow networks supports corrective steering**

477 A straightforward circuit for angular course control based on optic flow can be created
478 by connecting two rotational optic flow detectors (e.g., HS cells) separately to two rotational
479 actuators (e.g., DNp15). Such a system performs well when there is a significant difference in
480 activity levels between the two sensors. However, it performs poorly in detecting rotations
481 when the animal is moving forward at high speeds, which is surprisingly the condition where

482 HS cells contribute the most to corrective steering[35,36]. Furthermore, locomotion requires
483 continuous adjustments due to internal sources of noise, such as muscular and sensorimotor
484 noise, as well as uncertainties in the environment. These adjustments cause the optic flow to
485 be non-stationary, even when the fly intends to maintain a fixed course[72].

486 We propose two critical roles for the inhibitory motifs identified in the H2-HS network.
487 Firstly, it allows comparing the activity state of LPTCs across the two hemispheres and
488 provides cross-inhibition to silence competing inhibitory neurons, leading to a binary choice of
489 turning left or right. Similar circuit motifs with cross-inhibitory neurons in the hindbrain of
490 Zebrafish[73] and the vertebrate superior colliculus[74] bias angular movements in opposite
491 directions when activated or inhibited asymmetrically. Our experiments with bIPS yield
492 analogous results (**Fig. 6c**). Secondly, the inhibitory motifs can adjust the gain of LPTCs
493 during highspeed locomotion, allowing them to flexibly respond to changes in external and
494 internal conditions. Notably, bIPS provides prominent contralateral inputs to inhibitory
495 feedback CH cells, which project from the posterior slope back the lobula plate. CH cells
496 receive more than 450 synapses from bIPS (**Fig. 2-S1**). It is possible that bIPS corresponds
497 to the previously hypothesized *Horizontal unknown* cell, which provides binocular information
498 to CH cells through contralateral inhibition[75], thus playing a major role in integrating horizontal
499 motion from both eyes. Given its selectivity and inputs from motor and premotor regions, bIPS
500 is well suited for monitoring the fly's motor state, modulating descending neurons, feedback
501 pathways, and central pathways during periods of straightforward walking. This class of cells
502 also instructs optic flow processing, self-motion estimation and steering in the presence of
503 angular drifts. Therefore, bIPS contributes to the modulation of optic flow processing in a
504 multilayer manner.

505 **Estimation of self-motion from the eyes down to premotor and motor centers**

506 Optic flow-sensitive neurons have long been proposed to be integral components of
507 vital visuomotor circuits that enable animals to accurately perceive heading and control their
508 gaze and steering. In flies, while we have made substantial progress in understanding how
509 light reaching the photoreceptors are processed to detect visual motion and stimulate HS, H2,
510 VS cells and other LPTCs[28,76], our knowledge of how downstream pathways are organized
511 and process optic flow has remained far more limited. With the comprehensive description of
512 the HS, H2 and VS networks outlined here, and the visual and behavioral analysis of neurons
513 within these networks, we now possess a framework to establish mechanistic links between
514 visual activity in these networks and the ongoing locomotion control of a freely moving fly.
515 Given the common characteristics of optic flow and associated visual neurons processing
516 across different animal species[77,78] and the universal constrains on locomotive systems, the
517 findings reported here have the potential to shed light on how analogous systems in other
518 animals are functionally organized to process naturalistic optic flow in support of navigation.

519 Acknowledgements

520 We thank Ruchi Parekh and Janelia CAT for introducing us to FAFB and training us in EM
521 tracing. Kaylynn Coates and Feng Li for reviewing some of our manually traced neurons in
522 FAFB. Stephen Huston for early tracing of VCNMN and some cLPTCrn cells with Shahrozia
523 Imtiaz and for helping identify neck motor neurons. Anna Li and Rachel Wilson for their help
524 in reconstructing DNa02. Shigehiro Namiki and Gwyneth Card for their help in identifying
525 descending neurons. Jens Goldammer for identifying potential split-Gal4 candidates for H2rn
526 cells and helping identify S-Neurons. Hideo Otsuna, Greg Jefferis and Phillip Schlegel for
527 introducing us to their tools for computational neuroanatomy and for helping with EM data
528 analysis. Arthur Zhao for his input on LPTC naming and response predictions. Nils Eckstein
529 and Jan Funke for sharing neurotransmitter predictions for LPTC partners prior to publication.
530 Gaby Maimon and Cheng Lyu for sharing sytGCaMP7f flies prior to publication. Marion Silies

for sharing the UAS-GCaMP6f, UAS-FLP recombinant line. Ece Sönmez for help with testing Split-Gal4 combinations and help with validating FlpStop recombinants. CR Fly Platform for assisting fly stock generation, maintenance, and GABA stainings. Lalanti Venkatasubramanian for her help with the initial bIPS>TrpA1 behavior experiments. Terufumi Fujiwara for help with finding and testing potential Split-Gal4 combinations for H2rn and uLPTCrn and help with building the 2-photon calcium imaging. André Marques and Wynne Stagnaro for sharing unpublished work about multisensory processing in LPTCrn and bIPS cells. Past and present Chiappe Lab members for useful discussions and feedback on experiments and the manuscript. This work was supported by the Champalimaud Foundation and the research infrastructure Congento, LISBOA-01-0145-FEDER-022170. MECh is supported by European Research Council Starting Grant ERC-2017-STG-759782 537.

Author Contributions

In alphabetical order:

Davi D Bock: Generation of FAFB dataset and allowing access pre-publication. Resources & Data Curation.

Margarida Brotas: Reconstruction and review of 1st and 2nd order LPTC partners and cross-matching LPTC partners across EM datasets. Investigating differences in anatomy, connectivity, and neurotransmitter profile among LPTC partners.

M Eugenia Chiappe: Conceptualization. Methodology. Supervision. Resources. Funding acquisition. Writing – original draft. Writing – Review & Editing. Visualization.

Tomás Cruz: Design, running and analysis of DNp15>hsFLP,Kir experiments. Provide input, feedback and initial scripts to parse and analyze behavior data. Behavioral agent simulations with the modeled network.

554 **Mert Erginkaya**: Conceptualization. Reconstruction and review of LPTC synaptic
555 partners and some LPTCs in FAFB. Reconstruction and review of 2nd order
556 inputs/outputs of LPTC networks. Cross-matching LPTC partners across EM
557 datasets. Analysis of EM anatomy & connectivity. Generation of all transgenic lines.
558 GABA stainings (with the help of Fly Platform). Designing, performing, and analyzing
559 calcium imaging experiments. Design and analysis of behavior experiments.
560 Visualization of data and writing the paper.

561 **Aljoscha Nern**: Generation of transgenic lines that label LPTCrns. Re-injection of
562 uLPTCrn Gal4 line. Input for split candidates for bIPS. EM-LM cell identification and
563 naming for several cell types.

564 **Michael B Reiser**: Conceptualization. Reconstruction of LPTCs in FAFB and
565 proofreading LPTCs in FlyWire and Hemibrain (by Reiser Lab tracers). Naming
566 LPTCs. Help with generating optic flow stimulus patterns in LED arena (Software, from
567 Matthew Isaacson). Regular feedback on EM tracing status & priorities, and feedback
568 on calcium imaging experiments.

569 **Kathrin Steck**: Reconstruction and review of LPTC partners in FAFB. Reconstruction
570 and review of 2nd order inputs/outputs of LPTC networks.

571 **Filipa Torrão**: Investigating differences in connectivity among LPTC partners.
572 Analysis of local connectivity structure within bIPS dendrites (**Fig. 6-S2**)

573 **Nélia Varela**: Generation of transgenic lines that label bIPS, H2rn, H2, HS.
574 Immunostainings and images for several transgenic lines. Performing behavioral
575 experiments. Immunostainings for individual bIPS>hsFLP,Kir and DNp15>hsFLP,Kir
576 and MCFO flies.

Inclusion and Diversity Statement

While citing references scientifically relevant for this study, we worked to promote gender balance in our reference list as much as possible

Declaration of Interests

The authors declare no competing interests

Tables

Supplementary Table 1: Cross-matching of LPTC outputs across EM dataset

H2 Output Cells	FlyWire rank	FAFB rank	Hemibrain rank
PS047	3	1	3
VCH	1	2	2
DCH	2	3	1
DNp15	4*	4	4
bIPS	5	5	5
CNMNx	34*	6	11**
DNb03	6	7	7
DNb03	8	8	8
DNg41	9	9	6**
uLPTCrn	11	10	9
PS126	10	12	28
PS099	7	31	48
PS081	14	16	10
HS Output Cells	**FlyWire rank**	**FAFB rank**	**Hemibrain rank**
bIPS	1	1	2
DNp15	2*	2	1
PS047	4	3	3
CNMNx	21*	4	4**
VCNMN	5	5	7**
DNa02	3	6	9
uLPTCrn	10	7	5
lVLPT8	8	8	35
uLPTCrn	16	9	6
uLPTCrn	13	10	10
PLP195	6	11	29
DNgX	7	26	

DNa04			8
VS Output Cells	**FlyWire rank**	**FAFB rank**	**Hemibrain rank**
DNp20	1*	1	2
DNb06	2	2	
cLPTCrn	4	3	10
CNMN6	6	4	6
CNMN7	31	5	
cLPTCrn	7	6	20
uLPTCrn	40	7	5
PS126	3	8	7
S-Neuron	45	9	8
S-Neuron	38	10	9
DNge043	5	48	3
DNp22	8	70	
PS135	9	37	1
cLPTCrn	10	12	16
PS169	48		4

* FlyWire segmentation or synapse predictions are of low quality

** Uncertain hemibrain matching, since it is based on a small neural arbor cut off at the limits of the dataset

Supplementary Table 2: List of neurons within the LPTC central brain network

#	FAFB ID	FlyWire segment ID*	FlyWire soma coordinates	Hemibrain ID	Hemibrain cell type
1	Right uLPTCrn 2918805 PG ME	720575940628599516	114786, 73911, 1623		PS070-PS074
2	Right uLPTCrn 11965240 ME	720575940631296543	113632, 74374, 1687		PS070-PS074
3	Right DNg41 15463855 MB	720575940617611643	99290, 75988, 3794	5813024629**	
4	Right uLPTCrn 2549438 ME	720575940631333955	109930, 75338, 1666		PS070-PS074
5	Right uLPTCrn 2544668 ME	720575940612144047	112472, 73317, 1957		PS070-PS074

6	GNG neuron 2948699 ME	720575940648969337	121455, 91088, 2979		
7	DCH neuron (right) 1077175 ZSG-GA	720575940640039989	131955.27, 53517.50, 1223.00	1466485353	DCH
8	VCH neuron (right) 1078536 GA-ZSG	720575940627138562	134785, 53191, 958	5813024201	VCH
9	Putative CNMN 5218081 ME	720575940622008560***	105319, 78004, 4717	2180780757**	
10	VCN002 DB	720575940635776760***	124703, 91385, 3579	2428058771**	
11	DNa02_AL	720575940629327659	101150, 42526, 2117	1140245595	DNa02
12	neuron 7828867 BG	720575940621564329	104740, 50998, 5510		PLP195
13	DNgX 999559 ME	720575940614730914	105915, 76095, 4569	1874217622**	
14	Putative Right cLPTCrn 410927 SI	720575940642061709	112863, 73654, 2042		PS079
15	Right cLPTCrn 410809 SI	720575940617997396	113277, 73467, 2192		PS079
16	Right bLPTCrn 416268 ME	720575940608760110	112920, 74883, 1730		PS078
17	Right bLPTCrn 986687 ME	720575940620555696	111749, 73943, 2041		PS078
18	Right uLPTCrn 2500746 ME	720575940606873522	112559, 74568, 1653		PS070-PS074
19	Right uLPTCrn 1002426 ME	720575940647708537	114241, 73636, 1682		PS070-PS074
20	Right DNp15 5224930 ME	720575940610301413***	120043, 60033, 5393	5813078134**	DNp15
21	Right bIPS neuron 3029744 ME	720575940622581173	125645, 88652, 4814	1932497911	
22	Right PS047 16769498 ME	720575940638306163	98755, 67802, 2032	1621806893	PS047

23	Left bIPS neuron 969206 ME	720575940623618708	141214, 90010, 4743	1963869636	
24	H2 neuron (left) 5232903 ME	720575940632427603	164810, 54592, 5192	5813078454	H2
25	Right DNb03 8416446530 ME	720575940620776880	105915, 58345, 1981		DNb03
26	Right H2rn 11956981 ME	720575940621865991	127153, 91186, 3928		
27	Right DNb03 413171 MB	720575940634163682	107706, 58941, 2096		
28	Right H2rn 11930922 ME	720575940622082451	128029, 91037, 3888		
29	Right H2rn 9730354 ME	720575940624756836	126229, 90972, 3889		
30	Right H2rn 8438890 ME	720575940617566769	127758, 91886, 3927		
31	Right H2rn 8178074 ME	720575940642076576	127930, 91367, 4018		
32	Putative VSN 851433 ZSG	720575940624931564	89397, 61348, 6667	5813033533	VS
33	Putative VSN 804093 ZSG	720575940633923298	82426, 57153, 6848	1558230909	VS
34	neuron 5207415 ME	720575940613940074	83118, 55640, 4101	1221457679	IVLPT8
35	Putative HSN 830794 ZSG	720575940628031249	91612, 60674, 6567	2211443902	HSN
36	Putative HSE 827035 ECS ZSG	720575940642723981	98857, 55902, 5783	1807537598	HSE
37	Putative HSS 408972 SJH ZSG	720575940622312965	94341, 61845, 6407	2179731270	HSS
38	VSN-Like 982898 ZSG	720575940626477498	86531, 61966, 6790	5813024262	VS
39	putative VSN 793033 ZSG	720575940615269794	82514, 59151, 6836	1868619183	VS
40	Putative VSN 815777 ZSG	720575940622831740	84905, 55521, 6704	5813025091	VS

41	Putative VSN 852994 JLME ZSG	720575940633017939	82465, 56046, 6799	1557885051	VS
42	Putative VSN 807402 ZSG	720575940626457406	85387, 60389, 6811	1868255513	VS
43	putative VSN 804540 ZSG	720575940605688492	84584, 57582, 6777	1992161820	VS
44	Right S-Neuron 4906099 ME	720575940629666971	126241, 28340, 3824		OCG07
45	Right S-Neuron 4905400 ME	720575940625314547	127007, 30053, 4080		OCG07
46	Right S-Neuron 4880581 ME	720575940609826499	127788, 30884, 4072		OCG07
47	Right DNOVS1 9937342 ME	720575940629390123***	115510, 45447, 4960	1745333830**	DNp20
48	Right DNb06 9857697 ME	720575940637308605	126678, 68176, 1317	1715999506	DNb06
49	Right PS126 4905394 ME	720575940629701484	131516, 30646, 3039	1591156798	PS126
50	Left bLPTCrn 9157628 ME	720575940631876577	149420, 77362, 1632		PS078
51	Right bLPTCrn 17646150 ME	720575940624461543	113818, 75477, 1710		PS078
52	Right bLPTCrn 869476 ME	720575940628284931	113237, 74767, 1898		PS078
53	Putative Right bLPTCrn 1934541 ME	720575940605344434	113968, 76236, 1733		PS078
54	Cervical Nerve Neuron 1337778 SI	720575940633404627	118851, 65265, 5421		
55	Cervical Nerve Neuron 1167859 SI	720575940621583286	119957, 62874, 5368		
56	Left bLPTCrn 9369685 ME	720575940610505881	148617, 76818, 1461		PS078

57	Right cLPTCrn 968975 ME	720575940625557069	110736, 74923, 2028		PS079
58	Left cLPTCrn 414149 ME	720575940607991819	146347, 76067, 1244		PS079
59	Left cLPTCrn 2725485 ME	720575940629929273	147252, 76791, 1398		PS079
60	Left cLPTCrn 1006244 SI	720575940612306641	146666, 75707, 1607		PS079
61	Right cLPTCrn 414194 ME	720575940620867254	112846, 70948, 2282		PS079
62	Right cLPTCrn 1051520 SI	720575940629267531	111884, 74761, 2203		PS079
63	Left cLPTCrn 967831 ME	720575940624324708	147231, 75756, 1219		PS079
64	Putative Right cLPTCrn 9336219 ME	720575940631645009	111149, 73533, 1804		PS079
65	Left cLPTCrn 4881422 ME	720575940626420220	146247, 75467, 1279		PS079
66	Right cLPTCrn 969249 ME	720575940620263088	111942, 73451, 1739		PS079
67	Left cLPTCrn 952121 ME	720575940616362123	148068, 76482, 1602		PS079
68	Left cLPTCrn 412520 ME	720575940621845119	147390, 76088, 1339		PS079
69	Right cLPTCrn 2560372 ME	720575940628688246	113125, 72872, 1901		PS079
70	Right cLPTCrn 411566 ME	720575940619872751	113686, 72642, 2212		PS079
71	Left cLPTCrn 1027141 SI	720575940635634680	145378, 76025, 1378		PS079
72	Right cLPTCrn 968122 ME	720575940621147425	114031, 73227, 1620		PS079

* As of 230422

590 ** Uncertain hemibrain matching, due to incomplete hemibrain skeleton

591 *** Bad or incomplete segmentation in FlyWire

592 **Supplementary Table 3: List of fly lines used in each figure**

Figure(s)	Panel(s)	Target cell type(s)	Genotype(s)
1	d, e	DNp15	w^{1118}; R11E07-p65.AD / 20XUAS-jGCaMP7f; R77F05-Gal4.DBD / 20xUAS-6XmCherry; 13XLexAop-jGCaMP7f; R77F05-LexA; +;
1	f, g	DNp15	hsFLP; R11E07-p65.AD / +; R77F05-Gal4.DBD / 10XUAS>Stop>eGFPKir2.1;
1-S1		DNp15	w^{1118}; R11E07-p65.AD / 20XUAS-jGCaMP7f; R77F05-Gal4.DBD / 20XUAS-6XmCherry; 13XLexAop-jGCaMP7f; R77F05-LexA; +;
1-S1	f, g	DNp15	hsFLP; R11E07-p65.AD / +; R77F05-Gal4.DBD / 10XUAS>Stop>eGFPKir2.1;
1,1-S1,3,3-S2,3-S3		HS	w^{1118}; R27B03-p65.AD / 20XUAS-6XmCherry; R39E01-Gal4.DBD / UAS-sytGCaMP7f; w^{1118}; 20XUAS-jGCaMP7f / +; VT058487-Gal4 / UAS-CD4::tdTomato w^{1118}; R39E01-LexA, 13XLexAop2-6XmCherry / +; VT058487-Gal4 / UAS-sytGCaMP7f
3,3-S2,3-S3		H2	w^{1118}; R23C12-p65.AD / 20XUAS-6XmCherry; R32A11-Gal4.DBD / UAS-sytGCaMP7f; w^{1118}; R23C12-p65.AD / R39E01-LexA, 13XLexAop2-6XmCherry; R32A11-Gal4.DBD / UAS-sytGCaMP7f
3,3-S2,3-S3		bIPS	w^{1118}; R25F07-p65.AD / 20XUAS-6XmCherry; VT014724-Gal4.DBD / UAS-sytGCaMP7f; w^{1118}; R25F07-p65.AD / 20XUAS-jGCaMP7f; VT014724-Gal4.DBD / UAS-CD4::tdTomato
3,3-S2,3-S3		H2rn	w^{1118}; VT040346-p65.AD / 20XUAS-6XmCherry; VT049923-Gal4.DBD / UAS-sytGCaMP7f;
3,3-S2,3-S3		uLPTCrn	w^{1118}; 20XUAS-6XmCherry / +; R50G03-Gal4 / UAS-sytGCaMP7f; w^{1118}; R39E01-LexA, 13XLexAop-6XmCherry / +; R50G03-Gal4 / UAS-sytGCaMP7f
3-S1	a	bIPS	w^{1118}; R25F07-p65.AD / UAS-mCD8::GFP; VT014724-Gal4.DBD / +;
3-S1	a	H2rn	w^{1118}; VT040346-p65.AD / UAS-mCD8::GFP; VT049923-Gal4.DBD / +;

Figure(s)	Panel(s)	Target cell type(s)	Genotype(s)
3-S1	a	uLPTCrn	w^{1118}; Otd-nls:FLPo / +; R50G03-Gal4 / pJFRC56-10XUAS>Stop>eGFPKir2.1;
3-S1	a	LPTCrn	w^{1118}; VT045281-p65.AD / Otd-nls:FLPo; VT038829-Gal4.DBD / pJFRC56-10XUAS>Stop>eGFPKir2.1;
3-S1	a	HS	w^{1118}; R27B03-p65.AD / 20XUAS-jGCaMP7f; R39E01-Gal4.DBD / UAS-CD4::TdTomato;
3-S1	a	H2	w^{1118}; R23C12-p65.AD / UAS-2xEGFP; R32A11-Gal4.DBD / +;
3-S1	a	DNp15	w^{1118}; R11E07-p65.AD / 20XUAS-jGCaMP7f; R77F05-Gal4.DBD / 20XUAS-6XmCherry;
3-S1	b	LPTCrn	w^{1118} / MCFO-1; VT045281-p65.AD / +; VT038829-Gal4.DBD / MCFO-1;
3-S1	c	bIPS Rdl +/-	w^{1118}; R25F07-p65.AD / 20XUAS-GCaMP6f, UAS-FLP; VT014724-Gal4.DBD / $Rdl^{FlpStop\ ND}$;
3-S1	c	bIPS Rdl -/-	w^{1118}; R25F07-p65.AD / 20XUAS-GCaMP6f, UAS-FLP; VT014724-Gal4.DBD, $Rdl^{FlpStop\ ND}$ / $Rdl^{FlpStop\ ND}$;
4		bIPS Rdl +/+	w^{1118}; R25F07-p65.AD / 20XUAS-GCaMP6f, UAS-FLP; VT014724-Gal4.DBD / 20XUAS-6XmCherry;
4		bIPS Rdl -/-	w^{1118}; R25F07-p65.AD / 20XUAS-GCaMP6f, UAS-FLP; VT014724-Gal4.DBD, $Rdl^{FlpStop\ ND}$ / $Rdl^{FlpStop\ ND}$;
4-S1	a	LPTCrn	w^{1118}; VT045281-p65.AD / UAS-mCD8::GFP; VT038829-Gal4.DBD / +;
4-S1	a	uLPTCrn	w^{1118}; UAS-mCD8::GFP / + ; R50G03-Gal4 / +;
4-S1	a	bIPS	w^{1118}; VT014724-p65.AD / UAS-mCD8::GFP; VT039047-Gal4.DBD / +;
4-S1	a	H2rn	w^{1118}; VT040346-p65.AD / UAS-mCD8::GFP; VT049923-Gal4.DBD / +;
4-S1	b	LPTCrn ∩ GAD1	w^{1118}; UAS-mCD8::GFP / +; VT045281-Gal4.DBD / GAD1-p65.AD;
4-S1	b	LPTCrn ∩ ChaT	w^{1118}; VT045281-p65.AD / UAS-mCD8::GFP; ChaT-Gal4.DBD / +;
4-S1	b	LPTCrn ∩ VGlut	w^{1118}; VT045281-p65.AD / VGlut-Gal4.DBD; 40xUAS-mCD8::GFP;
4-S1	b	uLPTCrn ∩ GAD1	w^{1118}; UAS-mCD8::GFP / +; GAD1-p65.AD / R50G03-Gal4.DBD;
4-S1	b	uLPTCrn ∩ ChaT	w^{1118}; R50G03-p65.AD / UAS-mCD8::GFP; ChaT-Gal4.DBD / +;
4-S1	b	uLPTCrn ∩ VGlut	w^{1118}; R50G03-p65.AD / VGlut-Gal4.DBD; 40xUAS-mCD8::GFP;
4-S1	b	bIPS ∩ GAD1	w^{1118}; UAS-mCD8::GFP / +; GAD1-p65.AD / VT014724-Gal4.DBD;
4-S1	b	bIPS ∩ ChaT	w^{1118}; VT014724-p65.AD / UAS-mCD8::GFP; ChaT-Gal4.DBD / +;
4-S1	b	bIPS ∩ VGlut	w^{1118}; VGlut-p65.AD / UAS-mCD8::GFP; VT019845-Gal4.DBD / +;

Figure(s)	Panel(s)	Target cell type(s)	Genotype(s)
4-S1	b	H2rn ∩ GAD1	w^{1118}; UAS-mCD8::GFP / CyO; GAD1-p65.AD / VT049923-Gal4.DBD;
4-S1	b	H2rn ∩ ChaT	w^{1118}; VT040346-p65.AD / UAS-mCD8::GFP; ChaT-Gal4.DBD / +;
4-S1	b	H2rn ∩ VGlut	w^{1118}; VGlut-p65.AD / UAS-mCD8::GFP; VT049923-Gal4.DBD / +;
6	b	DNp15	hsFLP; R11E07-p65.AD / +; R77F05-Gal4.DBD / 10XUAS>Stop>eGFPKir2.1;
6	c	bIPS	hsFLP; R25F07-p65.AD / +; VT014724-Gal4.DBD / 10XUAS>Stop>eGFPKir2.1;
6	d	empty control >TrpA1 (control 1)	w^{1118}; Empty-p65.AD / UAS-TrpA1(B).K; Empty-Gal4.DBD / +;
6	d	bIPS #1 >TrpA1	w^{1118}; R25F07-p65.AD / UAS-TrpA1(B).K; VT014724-Gal4.DBD / +;
6	d	bIPS #2 >TrpA1	w^{1118}; VT014724-p65.AD / UAS-TrpA1(B).K; VT039047-Gal4.DBD / +;
6	d	bIPS #3 >TrpA1	w^{1118}; VT039047-p65.AD / UAS-TrpA1(B).K; VT019845-Gal4.DBD / +;
6	d	empty control > Kir2.1 (control 2)	w^{1118}; Empty-p65.AD / Otd-nls:FLPo ; Empty-Gal4.DBD / pJFRC56-10XUAS>Stop>eGFPKir2.1;
6	d	bIPS #1 > Kir2.1	w^{1118}; R25F07-p65.AD / Otd-nls:FLPo; VT014724-Gal4.DBD / pJFRC56-10XUAS>Stop>eGFPKir2.1;
6-S1	a	bIPS #1	w^{1118}; R25F07-p65.AD / UAS-mCD8::GFP; VT014724-Gal4.DBD / +;
6-S1	a	bIPS #2	w^{1118}; VT014724-p65.AD / UAS-mCD8::GFP; VT039047-Gal4.DBD / +;
6-S1	a	bIPS #3	w^{1118}; VT039047-p65.AD / UAS-mCD8::GFP; VT019845-Gal4.DBD / +;
6-S1	b	bIPS	hsFLP; R25F07-p65.AD / +; VT014724-Gal4.DBD / pJFRC56-10XUAS>Stop>eGFPKir2.1;

Figure legends

Figure 1: DNp15 exhibit enhanced sensitivity to rotational optic flow compared to HS and plays a role in steering during high-speed translation (**a**) Simulated binocular optic flow of a fly walking at low (left) versus high (right) forward speed and rotating with the same angular velocity. Rectangles indicate the presence of regressive (blue) or progressive (magenta) motion detected by a horizontal motion-sensitive system. (**b**) EM-reconstructed

600 right HS (magenta) and postsynaptic right DNp15 (olive) cells. The chemical and electrical
601 synapses between the two cells allocated within the inferior posterior slope (IPS, cyan), a
602 premotor region. The dendrites of HS cells are located within the lobula plate (LP). (**c**) Top,
603 schematic of the fly brain and the IPS, where optical imaging was performed. Bottom, 2-
604 photon calcium imaging setup and the visual LED display. (**d**) HS (magenta) and DNp15
605 (olive) calcium responses to horizontal binocular rotational or translational-like optic flow (top),
606 and to monocular optic flow (bottom). (e) Discrimination index (see **Methods**) between
607 translational-like and rotational stimuli in HS (magenta) and DNp15 (olive). Each circle
608 represents an individual ROI. Colored horizontal line and black vertical line represent the
609 mean and 95% CI. (HS: N=12 flies, n=16 ROIs, DNp15: N=6 flies n=7 ROIs, *P < 0.05; **P <
610 0.01 ***P < 0.001, Wilcoxon's rank-sum test). (**f**) The walking paths of forward runs of length
611 ≥ 4 body lengths, aligned at their origin, in flies with either both or none DNP15 silenced (left,
612 light gray traces), right DNP15 silenced (middle, gray traces), and left DNP15 silenced (right,
613 black traces). (**g**) Left, definition of path deviation, the difference in body orientation between
614 the end and the beginning of the walking path over traveled distance. Right, mean path
615 deviation from per fly in flies with none, single or both DNp15 silenced. The size of the circle
616 indicates the number of walking bouts per fly, with larger sizes representing larger number of
617 walking bouts. Number of flies per condition, none n=25; both n=31; left n=22; right n=22; *p
618 < 0.05 **p < 0.01 ***p < 0.001, Wilcoxon's rank-sum test with Bonferroni correction for multiple
619 comparisons.
620
621 **Figure 2. H2, HS and VS cells form two distinctive networks in the central brain.** (**a**)
622 Connectivity graph of the H2-HS (left) and VS (right) networks. Neurons are represented as
623 nodes (circles), with their synaptic connections indicated by arrows (predicted to be excitatory)
624 or circled edges (predicted to be inhibitory). Thickness of the arrows/circled edges represents
625 number of synapses, and color indicates the presynaptic neuron. For clarity, connections with

626 fewer than 10 synapses are not shown; connections with fewer than 50 synapses are shaded.
627 Node diameters represent the total number of connections that each node has within the
628 network (including both inputs and outputs). Except for LPTCs, nodes are placed within the
629 brain regions (grey rectangles) where their axons reside. (**b**) The total number of synaptic
630 connections for each neuron within H2-HS network (Top), and VS network (bottom). See
631 Supplementary Table 2 for the complete list of neurons and nomenclature. (**c**) Connectivity
632 graph between each LPTC input cell type and individual HS, H2 and VS cells. Edges indicate
633 synaptic connection between cells, with thickness indicating number of synapses and color
634 indicating the presynaptic cell. LPTCs without input are transparent for clarity.
635
636 **Figure 3: Binocular interactions define optic flow sensitivity in H2-HS interneurons.** (**a**)
637 Local connectivity between the input and middle layers of the H2-HS network. (**b**) Left,
638 schematic of the central nervous system (CNS) regions from which uLPTCrns, bIPS and
639 H2rns receive inputs. LOP, Lobula Plate; ME, Medulla; GNG, gnathal ganglia; IPS, inferior
640 poste-rior slope; SPS, superior posterior slope. Right, proportion of inputs per CNS region
641 (color code) for each interneuron. (**c**) Single plane fluorescence image of an example
642 recording from bIPS axons during binocular CW (top) and CCW (bottom) horizontal motion.
643 We defined a single region of interest (ROI), which covers the entire axon is outlined in white.
644 The red signal corresponds to mCherry fluorescence, whereas the green signal corresponds
645 to sytGCaMP7f fluorescence. Scale bar, 10 μm. (**d**) Top: visual stimuli presented to the fly,
646 with direction of motion as indicated by arrows. Bottom: optic flow calcium responses (OFR)
647 of each neuron to rotational (stimuli 1, 2, 3) or translational (stimuli 4, 5) optic flow. OFR for
648 rotational stimuli is defined as CW (rightwards) minus CCW (leftwards) direction of visual
649 motion. For the translational stimuli, OFR is defined as progressive minus regressive direction
650 of visual motion. Each trace corresponds to the grand mean of the z-scored calcium response
651 across flies ± SEM (shade). Per fly, we obtained mean responses to 5-10 repetitions per

652 stimulus. Light-gray rectangles indicate the stimulation window. For this and the remaining
653 panels: HS: N=12 flies n=16 ROIs, H2: N =8 flies n=11 ROIs, bIPS: N=10 flies n=11 ROIs,
654 H2rn: N=5 flies n=8 ROIs, uLPTCrn: N=6 flies n=8 ROIs. (**e**) Normalized OFRs (relative to the
655 preferred stimulus per neuron). Error bars represent SEM of the grand mean across flies. (**f**)
656 Left, discrimination index between translation-like vs. rotational stimuli (see **Methods**). Each
657 circle represents an individual ROI. The horizontal line and black vertical line represent mean
658 and 95% CI. Right, discrimination index between translation vs. rotational stimuli. *: $p < 0.05$;
659 **$p < 0.01$; ***$p < 0.001$, Wilcoxon's rank-sum test with Bonferroni correction for multiple
660 comparisons.
661
662 **Figure 4: GABAergic inhibition fine-tunes optic flow responses in bIPS.** (**a**) Right bIPS
663 input profile, grouped by their predicted primary neurotransmitter. Neurons shown in b) are
664 highlighted with colored lines. (**b**) Schematic of the local connectivity of the input and middle
665 layers of the H2-HS network. Inhibitory connections are shown as tee shaped edges. Blocking
666 Rdl receptors in bIPS using FLPStop disrupts fast GABAergic signaling onto bIPS (black
667 crosses). (**c**) Neural responses of wild-type (dark green) and Rdl-disrupted (light green) bIPS
668 cells to binocular asymmetric (left, rotational) and symmetric (right, translational-like) optic
669 flow (OF). Each trace corresponds to the grand mean ± SEM (shaded area) of z-scored
670 calcium responses obtained across flies. For each fly, mean responses to 5-10 repetitions per
671 stimulus were obtained from a single ROI at the axon terminals. Stimuli with a star indicate
672 area under the curve (auc) responses that are statistically different from wild type bIPS
673 recordings. (**d**) Same as **c**), but for translational optic flow. (**e**) OF responses, the difference
674 between the preferred and nulled direction responses (auc) for horizontal and progressive
675 visual motion. (**f**) Left, discrimination index between translational-like and rotational optic flow
676 of recorded neurons in c) (see **Methods**). Each circle represents an individual ROI. Colored
677 horizontal line and black vertical line represents mean and 95% CI. Right, discrimination index

between progressive and rotational optic flow. For all panels: bIPS: N=7 flies n=9 ROIs, bIPS Rdl-FLPStop: N=7 flies n=10 ROIs. *P < 0.05; **P < 0.01 ***P < 0.001, Wilcoxon's rank-sum test.

Figure 5: A lateral disinhibitory motif enhance asymmetries in neural activity across the right versus left hemisphere. (**a**) Schematic of the agent architecture: two sets of Reichardt detectors tuned to front-to-back (FtoB) or back-to-front (BtoF) motion detect the optic flow generated by a simulated walking fly (See **Methods**, **Fig. 5-S1**). The detected visual motion is processed by a network of nodes that mimic the core network motif of H2-HS network (**Fig. 3a**). The weights that connect the nodes are tuned based on a subset of measured visual responses (**Fig. 5-S1**). (**b**) Simulated and observed visual responses to monocular and binocular patterns of optic flow. Responses were matched to the maximal observed response. Observed responses are replotted from **Fig. 3-S2** and **Fig. 4c** (**c**) Visual response of modeled bIPS to symmetric or asymmetric binocular optic flow, and with or without a functional input from uLPTCrns. (d) Left: discrimination index of modeled and observed bIPS with or without a functional input from uLPTCrns. Right: observedd bIPS' discrimination index with or without functional GABAergic input (replotted from **Fig. 4f**). (**e**) Definition of the Asymmetry Index (AI) and two example conditions with low and high AI values. (**f**) Asymmetry index of simulated neurons (colored) in the full model (Control), under bIPS silencing (Without B), under uLPTCrn silencing (Without U) and under both bIPS and uLPTCrn silencing (With-out U+B). The dot size corresponds to the magnitude of the neural response. (**g**) Asymmetry index of simulated neurons (colored) in the full model varying the forward velocity of the agent. The shaded area corresponds to the range of velocities observed for forward runs in real exploratory flies (Cruz et al. 2021)[38].

703 **Figure 6: bIPS plays a role in steering control during highspeed walking**. (**a**) Example
704 walking paths of the agent (left) and the real fly (right) under prominent visual feedback. (**b**)
705 Simulated (left) and real fly (right) angular bias during forward runs (see **Methods**) with DNp15
706 activity perturbed bilateral or unilaterally. Transparent dots depict mean bias of individual flies,
707 black dots represent grand mean per genotype, weighted by the amount of walking bouts (dot
708 size). Error bars represent SEM. Number of flies per condition, None n=25; Left n=22; Right
709 n=22; Both n=31. (**c**) Same as b), but for bIPS. Number of flies per condition, None n=65; Left
710 n=26; Right n=38; Both n=13. For (**b**) and (**c**): *p < 0.05; **p < 0.01 ***p < 0.001, Wilcoxon's
711 rank-sum test with Bonferroni correction for multiple comparisons. (**d**) Left, simulated
712 straightness of the agent during forward runs (see **Methods**) with control (green), bilaterally
713 activated (dark green) or silenced (light green) bIPS cells. Right, straightness of control flies
714 (green), or flies with bilaterally activated (dark green) or silenced (light green) bIPS cells.
715 Number of flies per condition, empty control>TrpA1 n=25; bIPS#1>TrpA1 n=27;
716 bIPS#2>TrpA1 n=25; bIPS#3>Tr-pA1 n=29; empty control>Kir2.1 n=22; bIPS#1>Kir2.1 n=23.
717 (**e**) Summary of the findings. The middle layer of the H2-HS network supports steering by
718 enhancing the difference in the activity levels of the output layer across hemispheres. This
719 function is driven by a competitive disinhibitory motif that is well posed to be recruited at
720 highspeed walking. In this condition, binocular optic flow may contain prominent translational
721 components, possibly overshadowing rotational cues that are critical for course control. We
722 propose that the competitive disinhibition at the middle layer plays an important role in
723 modulating the output layer in a continuous and dynamic manner, leading to a more robust
724 estimate of the deviations from a straight course.

725 **STAR★METHODS**

726 **KEY RESOURCES TABLE**

Reagent or resource	Source	ID
Antibodies		
mouse anti-nc82 antibody	DSHB	RRID: AB_2314866
chicken anti-GFP antibody	Abcam	RRID: AB_13970
Rabbit polyclonal anti-GFP antibody	Thermo Fisher Scientific	Cat#A6455 RRID: AB_221570
rabbit anti-GABA antibody	Sigma	RRID: A2052
rabbit anti-DsRed antibody	Abcam	AB356483
goat Alexa-488 anti-chicken	Invitrogen	RRID: A11038
goat Alexa-594 anti-rabbit	Invitrogen	RRID: AB_150088
goat Alexa-633 anti-mouse	Invitrogen	RRID: AB_141431
Experimental Models: Organisms/Strains		
Drosophila UAS-2xEGFP	Bloomington Drosophila Stock Center (BDSC)	RRID: BDSC_6874
Drosophila UAS-mCD8::GFP	BDSC	RRID: BDSC_5137
Drosophila 40XUAS-mCD8::GFP	BDSC	RRID: BDSC_32195
Drosophila UAS-CD4::tdTomato	BDSC	RRID: BDSC_35837

Drosophila 20XUAS-6XmCherry in VK00018	BDSC	RRID: BDSC_52267
Drosophila 20XUAS-6XmCherry in attP2	BDSC	RRID: BDSC_52268
Drosophila 13XLexAop2-6XmCherry	BDSC	RRID: BDSC_52272
Drosophila MCFO-1[79]	BDSC	RRID: BDSC_64085
Drosophila 13XLexAop-jGCaMP7f	BDSC	RRID: BDSC_80910
Drosophila 20XUAS-jGCaMP7f	BDSC	RRID: BDSC_80906
Drosophila UAS-sytGCaMP7f	Gaby Maimon[80]	RRID: BDSC_94619
Drosophila 20XUAS-GCaMP6f, UAS-FLP	Molina-Obando et al.[81]	N/A
Drosophila hs-FLP	BDSC	RRID: BDSC_23649
Drosophila Otd-nls:FLPo	Asahina et al[82]	N/A
Drosophila 8XLexAop2-FLPL in attP40	BDSC	RRID: BDSC_90892
Drosophila pJFRC56-10XUAS>Stop>eGFPKir2.1 in attP2	Gerry Rubin	N/A
Drosophila UAS-TrpA1(B).K	BDSC	RRID: BDSC_26263
Drosophila Rdl$^{\text{FlpStop ND}}$	BDSC	RRID: BDSC_67682

Drosophila VT014724-Gal4.DBD, RdlFlpStop ND	this study	N/A
Drosophila GAD1-p65.AD	BDSC	RRID: BDSC_60322
Drosophila VGlut-p65.AD	BDSC	RRID: BDSC_82986
Drosophila VGlut-Gal4.DBD	Diao et al. 2015[83]	N/A
Drosophila ChaT-Gal4.DBD	BDSC	RRID: BDSC_60318
Drosophila R12E04-LexA	BDSC	RRID: BDSC_52447
Drosophila R39E01-LexA	BDSC	RRID: BDSC_52776
Drosophila R39E01-LexA,13XLexAop2-6XmCherry	this study	N/A
Drosophila R77F05-LexA	BDSC	RRID: BDSC_54265
Drosophila Empty-Gal4	BDSC	RRID: BDSC_68384
Drosophila R50G03-Gal4	Aljoscha Nern	N/A
Drosophila VT058487-Gal4	Vienna Drosophila Resource Center (VDRC)	N/A
Drosophila w^{1118}; R11E07-p65.AD; R77F05-Gal4.DBD	BDSC	RRID: BDSC_75953

Drosophila w^{1118}; Empty-p65.AD; Empty-Gal4.DBD	BDSC	RRID: BDSC_79603
Drosophila R23C12-p65.AD	BDSC	RRID: BDSC_70130
Drosophila R25F07-p65.AD	BDSC	RRID: BDSC_70622
Drosophila R27B03-p65.AD	BDSC	RRID: BDSC_70164
Drosophila R50G03-p65.AD	Aljoscha Nern	N/A
Drosophila VT014724-p65.AD	BDSC	RRID: BDSC_72019
Drosophila VT039047-p65.AD	BDSC	RRID: BDSC_73268
Drosophila VT040346-p65.AD	BDSC	RRID: BDSC_74542
Drosophila VT045281-p65.AD	BDSC	RRID: BDSC_75164
Drosophila R32A11-Gal4.DBD	BDSC	RRID: BDSC_69228
Drosophila R39E01-Gal4.DBD	BDSC	RRID: BDSC_70217
Drosophila R50G03-Gal4.DBD	Aljoscha Nern	N/A
Drosophila VT014724-p65.DBD	BDSC	RRID: BDSC_72146
Drosophila VT019845-Gal4.DBD	BDSC	RRID: BDSC_73315
Drosophila VT038829-Gal4.DBD	BDSC	RRID: BDSC_73679
Drosophila VT039047-Gal4.DBD	BDSC	RRID: BDSC_73724
Drosophila VT045281-Gal4.DBD	BDSC	RRID: BDSC_72221

Drosophila VT049923-Gal4.DBD	BDSC	RRID: BDSC_73921
Software and Algorithms		
MATLAB	MathWorks, Inc.	RRID:SCR_001622
R	Open-source	RRID:SCR_001905
natverse[84] (R package)	Open-source	https://github.com/natverse
ScanImage	Vidrio Technologies	RRID:SCR_014307
Gephi	Open-source	RRID:SCR_004293
Fiji	Open-source	RRID:SCR_002285
CATMAID	Open-source	RRID:SCR_006278

727 **CONTACT FOR REAGENT AND RESOURCE SHARING**

728 All data and analysis code are available upon request directed to Eugenia Chiappe
729 (eugenia.chiappe@neuro.fchampalimaud.org).

730 **EXPERIMENTAL MODEL AND SUBJECT DETAILS**

731 **Drosophila husbandry**

732 *Drosophila melanogaster* were reared on a standard fly medium and kept on a
733 12hr light/12hr dark cycle at 25 ºC. All experiments were performed with 2-to-4-days
734 old flies. Calcium imaging experiments were carried out with female and behavior
735 experiments with male flies. The complete set of transgenic flies and their specific

736 sources are listed in the *Key Resources Table*. Full genotypes of flies used in each
737 experiment are described in **Supplementary Table 3**.

738 **METHOD DETAILS**

739 **Generation of recombinant lines**

740 For the R39E01-LexA,13xLexAop-6xmCherry recombinant, transgenic lines
741 carrying R39E01-LexA and 13xLexAop-6xmCherry were crossed according to
742 standard procedures. Putative recombinant progeny was scored based on eye color
743 and ectopic mCherry labeling in the ventral cuticle and verified by immunostaining.

744 For the VT014724-p65.DBD, $Rdl^{FlpStopND}$ recombinant, we could not use eye
745 color since FlpStop cassette does not contain the *mini-white* gene. We generated
746 stable lines from single progeny and verified recombinant lines using PCR, with
747 primers targeting the FLPStop cassette in the ND orientation as in[53].

748 **EM datasets and neuron identification**

749 **EM datasets**

750 Two different EM datasets were used: A full female adult *Drosophila* brain
751 imaged using serial section transmission EM (FAFB[40]) and another, dense
752 reconstruction of a partial adult female brain imaged using FIBSEM (focused ion-beam
753 scanning electron microscopy), referred to as Hemibrain[42]. In FAFB, neuron skeletons
754 were either manually traced using CATMAID[85,86], following the procedure described
755 in[40] or automatically segmented within the FlyWire[41] environment together with
756 chemical synapse predictions[87]. None of the EM datasets contain information about
757 electrical synapses (i.e., gap junctions).

758 **Neural reconstructions**

759 Manual tracing of neurons for ‘identification’ and for ‘completion’ has been done
760 in FAFB as described in[88]. Briefly, reconstructing the full arbor of a neuron results in
761 tracing for ‘completion’, while tracing the soma and the major axonic and dendritic
762 branches that contain microtubules results in tracing for ‘identification’. Tracing for
763 identification saves considerable tracing time by leaving out the many small,
764 microtubule-less branches called twigs. This strategy is often enough to uniquely
765 identify a neural class. For many FAFB neurons, we were able to readily obtain
766 complete reconstructions in FlyWire with small differences in their twigs. Some
767 neurons, however, were badly segmented in earlier instances of FlyWire and had to
768 be reconstructed manually in FAFB. For example, DNp15 neurons have a darker
769 cytosol and very striated dendritic branching, which resulted in incomplete automatic
770 segmentation and connectivity in FlyWire and Hemibrain datasets. Therefore, we
771 manually traced Right DNp15 for completion and performed input profile analysis on
772 the FAFB dataset (**Fig. 2-S3f**). HS, VS and H2 cells were all traced to completion.
773 Strong LPTC partners were traced for identification, most of which were then traced
774 to completion.

775 A recent connectome analysis of the three EM datasets found that the FAFB
776 dataset is left-right inverted[89]. This means the Right hemisphere neurons we
777 reconstructed in FAFB/FlyWire are actually the Left neurons in real world coordinates.
778 Since inter-hemisphere connectivity is highly stereotyped within and across EM
779 datasets[89], and doesn’t affect any of the results we present here in this study, we
780 retain the inverted naming of neurons reconstructed in FAFB. This allows for a more

781 intuitive comparison of with the Hemibrain dataset, which largely encompasses the
782 Right side of the brain.

783 **Tracing synaptic connections**

784 In addition to their anatomy, we have tagged the locations of all incoming
785 (postsynaptic) and outgoing (presynaptic) chemical synapses of HS, VS, H2 cells and
786 several classes of strong LPTC partners in FAFB. As a rule, we tagged all synaptic
787 connections between any pair of traced neurons. Therefore, even if a neuron does not
788 have all their synapses tagged, we obtain the total number of synaptic connections
789 between all neurons in our FAFB dataset, provided they are fully, or near-fully traced.

790 **Selection of LPTC partners to reconstruct**

791 We traced all HS, all H2 and >90% of VS inputs for identification (Fig. 1-S2c).
792 For LPTC outputs, which are ~10x more numerous than inputs, we chose a pseudo-
793 random sampling approach. In FAFB, most of the strongly connected partners make
794 multiple axo-dendritic connections around the same presynaptic bouton. We focused
795 on neurons that send multiple dendrites to LPTCs within a small area by visual
796 inspection. We then prioritized tracing these 'putative strong' partners for identification.

797 In addition, we checked the strongest LPTC partners in Hemibrain and FlyWire
798 datasets and reconstructed them in FAFB if they weren't traced for identification
799 already. This allowed us to reconstruct all of the strongest LPTC partners with minimal
800 manual tracing.

801 **EM to Light Microscopy (LM) matching**

802 We used natverse R libraries[84], in particular *templatebrains* and *rcatmaid* to
803 register FAFB neurons onto a common template (JFRC2010) that's used in large

804 driver line libraries curated by the Janelia FlyLight team[90–92]. We then transformed our
805 aligned FAFB skeletons onto a 2-D ColorMIP image[93] and ran a similarity search
806 between our neurons and Gal4 lines within FlyLight. Gal4 lines with high similarity
807 were shortlisted by manual inspection. The shortlisted lines were then used in
808 combinations to generate the Split-Gal4 lines with sparse expression[94]. Stability and
809 sparseness of each split combination was assessed by checking GFP expression of
810 several brains under a confocal microscope.

811 **Immunohistochemistry**

812 **Immunostainings and microscopy**

813 2-4 days old adult *Drosophila melanogaster* brains were dissected in
814 phosphate buffer saline (PBS). Immunostaining protocol was slightly modified from[95]
815 as follows: After dissection, brains were fixed with 4% paraformaldehyde (PFA)
816 diluted in PBS for 20 minutes in room temperature (or 1 hour on ice). Before the
817 application of the primary antibodies, brains were incubated for 15 minutes in 10%
818 normal goat serum (or 1 hour in 5% normal goat serum) with 0.1% Triton X-100 in
819 PBS.

820 For checking GFP and GCaMP expression, Chicken anti-GFP (Abcam, CAT
821 #ab13970, 1:1000 dilution) was used with Mouse anti-nc82 (Developmental Studies
822 Hybridoma Bank, 1:10 dilution). In flies that additionally express TdTomato or
823 mCherry, Rabbit anti-DsRed (Abcam, CAT #ab356483, 1:500) was also used. For
824 GABA stainings, Chicken anti-GFP was used together with Rabbit anti-GABA (1:100;
825 Sigma-Aldrich CAT #A2052). Secondary fluorescent antibodies were AlexaFluor594
826 Goat anti-Rabbit (Abcam, CAT #ab150088, 1:500), AlexaFluor488 Goat anti-Chicken

827 (Abcam, CAT #ab150173, 1:500), AlexaFluor633 Goat anti-Mouse (Life
828 Technologies, CAT #A-21050, 1:500). In a small number of immunostainings, Rabbit
829 anti-GFP and AlexaFluor488 Goat anti-Rabbit were used instead.

830 Confocal sections were acquired using a Zeiss LSM710 confocal microscope
831 at 1 or 2 μm intervals and maximum projections of image stacks were performed in
832 Fiji/ImageJ (https://imagej.net/software/fiji/).

833 **Calcium Imaging**

834 **Fly preparation for immobilized calcium imaging**

835 2-4 days old adult female flies were used in all experiments. To keep their body
836 size relatively constant, 2-6 flies were anaesthetized with CO_2 after eclosion and
837 housed in vials. On the day of imaging, to minimize the potential influence of sensory
838 reafference signals coming from the limbs, flies were cold-anaesthetized, and their
839 legs were removed using fine forceps from the femur-tibia joint for the forelegs and
840 coxa-femur joint for the middle and hind legs. The femur of the forelegs were kept
841 intact since it proved difficult to reliably wax the coxa without waxing the eyes and the
842 proboscis. Openings in all the legs were then covered with beeswax. Proboscis was
843 gently extended using fine forceps and waxed from below to minimize the movement
844 of the brain during imaging. The fly was mounted on a custom-made physiology holder
845 by temporarily pinning the thorax onto a small tungsten wire (A-M Systems #716100)
846 using UV-cured glue (Bondic). The mounting is aided by a custom-built
847 micromanipulator and a triple camera array to position the head in the same
848 orientation across flies. After each experiment, high resolution images of the fly head
849 from the side and bottom were taken to measure the head pitch, yaw and roll angles

850 as described in[50]. Once the desired head orientation is achieved, the fly head and the
851 body were waxed onto the physiology holder, and the UV-glued pin was removed. The
852 cuticle from the back of the head was removed with extra sharp forceps (Dumont 5SF).
853 Fat body tissues were removed by gentle suctioning while trachea and the muscles 1
854 and 16 of the fly head were removed by fine forceps. In this preparation, flies have no
855 mobility in their legs and proboscis, very limited mobility in their wings and abdomen,
856 and high mobility in their halteres and antennae.

857 **Imaging setup**

858 Flies ready for imaging were mounted under an upright microscope (Movable
859 Objective Microscope, Sutter) with a 40× water-immersion objective lens (CFI Apo
860 40XW NIR, Nikon). Calcium imaging was performed with a custom-built galvo-galvo
861 2-photon laser scanning system. We used a Chameleon Ultra II Ti-Sapphire
862 femtosecond laser (Coherent) tuned to 930 nm for GCaMP and tdTomato excitation
863 (6 mW under the objective lens) and 780 nm for mCherry excitation when available.
864 The longer excitation wavelength is not visible to the fly. Emission was collected on
865 GaAsP PMT detectors (Hamamatsu, H10770PA-40) through a 535/50 nm bandpass
866 filter for the green channel and 605/70 nm for red channel (Chroma). A 128x128 pixels
867 slice image was acquired with ScanImage at the dorsal part of the posterior slope,
868 where the axon terminals of all neurons that were imaged overlap. To record activity
869 in a consistently large region across different cell types, the acquisition frame rate
870 varied between 12.2-15.0 Hz. When mCherry or tdTomato was co-expressed with
871 GCaMP, higher resolution 3D z-stacks were taken of the imaged regions before or
872 after each experiment. The external solution, which perfused the preparation

873 constantly in room temperature, contained 103 mM NaCl, 3 mM KCl, 5 mM TES, 8
874 mM D-trehalose, 10 mM D-glucose, 26 mM $NaHCO_3$, 1 mM NaH_2PO_4, 4 mM $MgCl_2$
875 and 2 mM $CaCl_2$ in MilliQ water (270–275 mOsm) and was bubbled with 95% O_2 / 5%
876 CO_2 (pH ~7.3).

877 **Visual display**

878 The visual display consists of a 32 × 96 array of blue light-emitting diodes
879 (LEDs, 465 nm, Bright LED Electronics) that are modeled after Generation 3 (G3)
880 modular display[96] with four layers of blue filter (Rosco R385) to minimize light leaking
881 into photomultiplier tubes used in calcium imaging. For a centrally positioned fly, its
882 visual field subtended 216° in azimuth and 72° in elevation (pixel size of 2.25°). In an
883 initial set of experiments, we prepared flies for imaging and measured the head pitch
884 angle as described in[50]. The display was tilted 74° relative to the horizon to match the
885 average pitch angle of the imaged flies.

886 **Visual stimuli**

887 Starfield stimuli[97] were generated using MATLAB (MathWorks, Natick, MA)
888 scripts (from https://github.com/misaacson01/Motion_Maker_G4), which were slightly
889 modified to be compatible with the G3 display. We virtually extended our display onto
890 a 2D spherical volume and populated this volume with 500, equally sized dots (5° solid
891 angle diameter) at random and uniformly distributed positions. We illuminated the
892 pixels on the LED display that overlapped with the dots in this spherical volume.
893 Instead of having fully on/off edges, we used 16 gray-scale intensity levels which
894 allowed for edges in visual patterns to appear to move more smoothly across frames.
895 This increases the apparent resolution of the display while minimizing motion-

896 independent flicker responses in recorded neurons. All dots had a nominal contrast of
897 100%.

898 Each trial consists of an identical, stationary visual pattern shown to the fly,
899 followed by clockwise and counterclockwise movements of the pattern in a particular
900 body axis of rotation (pitch, yaw, and roll) or movements of the pattern in translational
901 axes (thrust and sideslip) that lasts for 2 seconds, flanked by stationary periods. Each
902 trial lasted for 13 seconds (still-motion-still-motion-still for 2-2-5-2-2 seconds) with 5
903 seconds of inter-trial interval where the visual display was unlit (dark). See
904 **Supplementary Video 1** for all optic flow patterns. In speed tuning experiments, only
905 one direction of motion was presented, as such, trials lasted for 6 seconds (still-
906 motion-still for 2-2-2 seconds). See **Supplementary Video 2** for speed tuning stimuli.
907 Every visual pattern was shown 3-12 times for each fly, and the order of the trials were
908 randomized.

909 **Choice of calcium indicators**

910 We initially tested several GCaMP variants to reliably record calcium activity
911 across all the cell types imaged in this study. We found sytGCaMP7f[80] to give us the
912 strongest signal-to-noise ratio across most cell types. In addition, sytGCaMP7f
913 guarantees imaging from the axon terminals, which allowed us to confidently
914 distinguish calcium activity coming from Right bIPS axons versus Left bIPS dendrites.
915 Therefore, we used sytGCaMP7f in most of our recordings. DNp15 does not have
916 axon terminals in the brain, so we used cytoplasmic GCaMP7f[98] instead. In FLPStop
917 experiments we used cytoplasmic GCaMP6f[99] which was readily recombined with
918 UAS-FLP and used in FlpStop experiments previously[81]. In these experiments, we

919 distinguished dendritic and axonic signals in bIPS using the anatomical landmarks
920 provided by TdTomato expression as well as the direction selectivity of the recorded
921 ROIs.

922 **Data acquisition and alignment for imaging**

923 Before quantifying fluorescence intensities, imaging frames were motion-
924 corrected in MATLAB by translating each frame in the x and y plane using efficient
925 subpixel image registration[100] to match the time-averaged template from that session.
926 Multiple recordings from the same fly were registered to the same template if the
927 positional shift between recordings was small. In a small number of flies the analysis
928 was performed on raw image traces, where the movement correction resulted in
929 abnormal shifts of imaging frames in most of the trials despite negligible brain
930 movement. All trials where the imaged neurons move out of the imaging plane were
931 discarded.

932 **Behavior**

933 **Exploratory walking arena**

934 The virtual reality setup used in the exploratory walking experiments has been
935 previously described[38]. Briefly, single 2-4 days old male flies with their wings clipped
936 since eclosion walked freely in a 90 mm circular arena with heated walls. We either
937 let the flies walk in darkness or projected a set of visual worlds that translate together
938 with the fly using real-time tracking of the fly's center of mass and orientation.

939 To label single bIPS or DNp15 cells, flies were placed under 30°C heat shock
940 for up to 15 minutes after their wings were removed post-eclosion. The brains of these
941 flies were dissected immediately after each experiment to confirm cell labeling.

942 **Agent fly simulations**

943 A simulated rigid-body agent moved forward or executed a saccade in
944 alternating activity and immobility intervals (**Fig. 5-S1d**). The distribution of the length
945 of activity bouts was similar to the real flies' distribution[38]. The agent explored a
946 simulated 90 mm circular arena with hot walls. Saccades were modeled as highly
947 stereotyped rapid events in the angular velocity of the agent. The probability and
948 amplitude/direction of a saccade depended on the distance to the arena wall. The time
949 intervals within an activity bout without saccades were considered forward runs.
950 Forward runs had constant translational speed (20 mm/s) except in **Fig. 5f** where the
951 forward velocity was varied. During forward runs, non-zero slow rotations are
952 represented by an "injected" 1/f noise (η). The size of η was scaled by the parameter
953 'Noise Level' (w_{noise}) to match the straightness of real flies walking in dark (**Fig. 5-**
954 **S1f**).

955 Rotations of the agent are guided by a visual controller based on measured
956 visual flow from both eyes. In short, four channels containing arrays of a "two-
957 quadrant" type Hassenstein-Reichardt (HR) correlator detected self-generated visual
958 motion cues[101]. Self-generated visual stimuli were modeled first by high-pass filtering
959 the visual pattern at each spatial position (τ = 50ms). This was followed by a half-wave
960 rectification step. Next, the visual signal was low-pass filtered (first order, τ = 15ms),
961 and then multiplied with an unfiltered signal from a neighboring spatial location. This
962 was done twice in a mirror-symmetrical manner, followed by subtraction, yielding a
963 fully opponent direction-selective output signal, which was then scaled by the
964 parameter 'Visual Weight' (w_{visual}) to match straightness of real flies experiencing

visual motion cues (**Fig. 5-S1g**). The two eyes of the agent are represented by independent arrays of HR, each detecting progressive (FtoB) and regressive (BtoF) visual rotations. Combinations of progressive and regressive signals were then used to simulate the response profiles of HS and H2 cells.

$$HS_{right} = w_{HSPD} * FtoB_{right} - w_{HSNPD} * BtoF_{right} + w_{HSContra} * BtoF_{left}$$

$$H2_{right} = w_{H2PD} * BtoF_{right} - w_{H2NPD} * FtoB_{right} + w_{H2Contra} * FtoB_{left}$$

The weights for HS and H2 responses were adjusted based on a subset of horizontal visual motion responses obtained (**Fig. 5-S1a**). Following HS and H2, the intermediate layer of inhibitory neurons – bIPS (B) and uLPTCrns (U) was simulated according to the architecture outlined in **Fig. 5a**.

$$B_{right} = w_{HSB} * HS_{right} + w_{H2B} * H2_{left} - w_{UB} * U_{right}$$

$$U_{right} = w_{HSU} * HS_{right} + w_{H2U} * H2_{left} - w_{BU} * B_{left}$$

Like HS and H2, the weights for bIPS and uLPTCrn responses were also adjusted based on real visual responses (**Fig. 5-S1b**). Finally, all simulated neurons converge onto a simulated DNp15 modeled after the H2-HS network architecture in **Fig. 2**.

$$DNp15_{right} = w_{HSp15} * HS_{right} + w_{H2p15} * H2_{left} - w_{Up15} * U_{right} - w_{Bp15} * B_{left}$$

The weights for DNp15 were adjusted to match the measured horizontal visual motion responses in **Fig. 1-S1c** by iteratively changing the weights of the input layer (HS and H2) and then changing the weights of the intermediate layer (B and U). The final table of weights is presented in **Fig. 5-S1c**.

The agent's rotation depends on the activity difference between Left and Right DNp15.

$$V_{angular}\ (°/s) = w_{visual} * \left(DNp15_{right} - DNp15_{left}\right) + w_{noise} * \eta$$

988 Where w_{visual} , w_{noise} and η correspond to the visual weight, noise level and injected
989 1/f noise, respectively. In the current framework, neuronal silencing was mimicked by
990 turning the signal from specific neurons to zero, while activation was mimicked by
991 turning the signal from specific neurons to 0.1. Asymmetry indices (AI) were calculated
992 by comparing the activity between left and right neurons for each neural population:

993 $$AI_{neuron} = \frac{|Neuron_{left} - Neuron_{right}|}{|Neuron_{left}| + |Neuron_{right}|}$$

994 **Data analysis**

995 **EM connectivity matrices and synaptic clustering**

996 We used *natverse*[84] R libraries to load HS, VS and H2 cells from FAFB and
997 prune their dendritic arbor in the optic lobes, leaving only the central brain projections.
998 We then loaded the list of all their synaptic partners, and together with HS, VS and H2
999 cells, we generated an all-by-all connectivity matrix where each point corresponds to
1000 the number of synapses from a row neuron to a column neuron.

1001 To cluster the neurons that are more closely connected with each other, we
1002 first summed input and output synapses between each pair of neurons, thereby
1003 generating a symmetric connectivity table. We then binarized this table, setting all non-
1004 zero connections to 1. This prevents very strong pairwise connections to take over
1005 and distort network clustering. Conversely, it increases the weight of the weakest
1006 connections (i.e., <5 synapses). Therefore, we convert all weak connections to zero
1007 before binarization. We compute the distance matrix using this binarized connectivity
1008 and perform hierarchical clustering with Ward's method to generate the connectivity
1009 dendrogram in **Fig. 2-S1**. The dendrogram was used to reorder the initial connectivity
1010 matrix where neurons that are clustered together are placed next to each other. We

1011 also ran the same clustering analysis without binarization nor removing weak partners
1012 (**Fig. 2-S2**) to confirm the broad network structure does not critically depend on these
1013 subjective parameters.

1014 **Network connectivity graphs**

1015 After generating the clusters, neurons within each cluster are loaded in
1016 CATMAID[86]. Neurons that belong to the same class (largely based on anatomy) are
1017 grouped together, generating a graph structure where each node is a neuron class
1018 and directed edges between nodes represent the number of synaptic connections.
1019 The adjacency matrix of this graph structure is then imported to Gephi where the edge
1020 and node parameters (color, size etc.) are adjusted for better visualization. The end
1021 point shape of each edge was determined by their predicted primary
1022 neurotransmitter[52].

1023 To measure the prominence of a neural class within each subnetwork, we
1024 plotted the weighted degree, which is the total number of incoming and outgoing
1025 synapses for each node inside that subnetwork (**Fig. 2b**).

1026 **Anatomical clustering of LPTC inputs**

1027 To quantify the anatomical similarities among LPTC input cell types (**Fig. 2-**
1028 **S3d**), we performed NBLAST[102] on the main backbone (primary neurite tracts with the
1029 primary dendrites) of LPTC input neurons. The smallest distal dendrites (twigs) were
1030 removed since they are highly variable and make NBLAST less sensitive to the
1031 stereotyped features of cells. Hierarchical clustering was then performed on Euclidean
1032 distance matrices of NBLAST scores using Ward's method.

1033 **Synaptic input profiles**

1034 To plot the neuropil input profile of LPTC input neurons (**Fig. 2-S3e, Fig. 3c**),
1035 we first obtained the list of upstream partners from FlyWire for each cell type. We only
1036 analyzed predicted synaptic sites with a cleft score of >50 to minimize false positives.
1037 We defined the input neuropil of each upstream cell as the brain region that houses
1038 most of their postsynaptic (dendritic) sites. Upstream cells that lack a soma or have
1039 less than 200 postsynaptic sites were visually inspected. The ones that project to the
1040 neck connective were scored as VNC/Neck. The remaining fragments without a cell
1041 soma were excluded from the analysis. For the DNp15 input profile (**Fig. 2-S3f**) we
1042 fully reconstructed Right DNp15 in FAFB and manually tagged all its synapses since
1043 it was badly segmented in FlyWire. We then traced ~89% of its synaptic partners for
1044 identification and defined their primary input neuropil. To plot the neurotransmitter
1045 input profile of bIPS (**Fig. 4a**) we regrouped the list of Right bIPS input neurons based
1046 on their predicted neurotransmitter[52].

1047 **Distance-to-root and inter-synaptic distance analyses on bIPS**

1048 We retrieved the spatial distribution of Right bIPS inputs from FAFB using
1049 *natverse* R libraries[84]. The location of each input synapse from Right HS, H2rn,
1050 uLPTCrn and Left H2 cells were projected onto a graph representation of bIPS neuron
1051 using *nabor* library. We defined the root point of bIPS as the soma-axon-dendrite
1052 junction, which is where all the dendritic arbors of bIPS converge before crossing the
1053 midline (**Fig. 4-S2a**). We then computed the geodesic distance between each input
1054 synapse and the root point using *igraph* library (**Fig. 4-S2b**). This analysis is loosely
1055 based on the electrotonic distance analysis within EPG neurons performed by Hulse

1056 et. al.[103]. Geodesic distances between H2rn inputs and the nearest H2 or HS input
1057 were calculated in a similar manner (**Fig. 4-S2c**).

1058 **Proportion of local circuitry motifs**

1059 The non-random locations of bIPS input synapses suggest they may be
1060 organized in distinct microcircuits as they contact bIPS. We assumed only one
1061 synaptic input from a presynaptic cell takes part in a microcircuit. We therefore defined
1062 1.865 μm as the maximum inter-synapse distance (**Fig. 4-S2c**, black line) based on
1063 the distances between H2rns with H2. We then counted the number of times a cell
1064 type (cell X) forms a microcircuit with H2 (**Fig. 4-S2d** and **4-S2f**) or HS (**Fig. 4-S2e**
1065 and **4-S2g**) as they give input to bIPS (**Fig. 4-S2d-e**) or DNp15 (**Fig. 4-S2f-g**),
1066 normalized by the total number of occurrences per motif.

1067 **Calcium responses to visual motion**

1068 After each imaging session, we manually defined regions of interest (ROI) that
1069 correspond to the axon terminals or dendrites of recorded neurons. For lines that label
1070 single neurons (e.g., H2, bIPS), only one ROI was defined. For lines that label multiple
1071 neurons, multiple ROIs were first defined. After confirming the visual responses of
1072 different ROIs were not qualitatively different, we chose a single ROI with the largest
1073 signal-to-noise ratio to represent the cell type. As such, we recorded the responses of
1074 no more than two ROIs per fly, one per hemisphere.

1075 To calculate calcium evoked responses in these ROIs, we calculated mean
1076 pixel intensity (fluorescence) for each trial (F). Baseline fluorescence (F_0) was defined
1077 as the F value of the last second before the first visual motion presentation. Change
1078 in calcium response was measured as:

1079 $\Delta F = F - F_0$

1080 Since $\Delta F/F$ measurements of calcium activity could create positive artifacts
1081 following negative deviations from baseline observed in several cell types we
1082 imaged[104], we instead Z normalized the ΔF data to compare optic flow responses
1083 within and across cell types. We downsampled the imaging data from each fly to the
1084 lowest recorded frame rate (12.2Hz). Recordings from left hand side cells were flipped
1085 to match the responses from right side recordings (and vice versa for H2 recordings).
1086 Matching is done by converting the stimulus identity (e.g. Roll clockwise, Pitch down
1087 and Yaw left) into its midline-symmetric version (Roll counter-clockwise, Pitch down
1088 and Yaw right), similar to what is described in Weir et al.[97]. Finally, all repetitions of a
1089 given stimulus were averaged to get a single mean response per stimulus per ROI.

1090 **Optic flow response indices**

1091 To measure the relative sensitivity of a neuron to a particular pattern of optic
1092 flow, we calculated the response as the area under the curve (auc) during the entire
1093 2 seconds of visual motion stimulation or calculated the mean response within the last
1094 200 ms of visual motion (peak). The preferred (PD) and non-preferred (NPD) direction
1095 of visual motion for all axes of movement were defined based on Right HS cell
1096 responses. Optic Flow (OF) responses (**Fig. 3c**) were plotted as the difference
1097 between calcium responses of the preferred (PD) and non-preferred (NPD) direction
1098 related to a given stimulus (e.g., CW minus CCW). The OF responses in **Fig. 3d** were
1099 normalized by the peak OF response per ROI.

1100 To measure the discrimination index (DI), we first calculated the peak OF
1101 response for a given optic flow pattern (e.g., Yaw). Here, PD and NPD responses were
1102 defined per cell type:

1103 $OF_{Yaw} = Peak_{PD} - Peak_{NPD}$

1104 The DI between two optic flow patterns (e.g., Progressive and Yaw) is
1105 calculated as the difference between OF values divided by the sum of the absolute
1106 OF values:

1107 $$DI = \frac{OFProg - OFYaw}{||OFProg|| + ||OFYaw||}$$

1108 **Classification of walking paths, walking straightness, and angular deviations**

1109 Walking paths are classified into spike-like saccadic events that correspond to
1110 rapid turns and forward segments as described in Cruz et al.[38]. Straightness of forward
1111 segments are calculated by first measuring local deviations from an ideal path within
1112 a running window of 333 ms for each point of the fly trajectory. Straightness is defined
1113 as the total distance traveled within each window divided by the sum of local
1114 deviations. Angular path deviation for each forward segment is defined as the
1115 cumulative angular deviation of the body divided by the total distance traveled.
1116 Angular bias is the binarized version of angular path deviation (**Fig. 1g, 5-S1e**).

1117 **QUANTIFICATION AND STATISTICAL ANALYSIS**

1118 **Statistics**

1119 We performed a two-sided Wilcoxon rank-sum (here, abbreviated as MWW)
1120 test for comparisons between two independent groups with Bonferroni correction for
1121 multiple comparisons where applicable.

1122

DATA AND CODE AVAILABILITY

Analysis codes and data in this paper are available upon request to the Lead Contact.

Supplementary figure and video legends

Figure 1-S1: DNp15's responses to optic flow and their effect on body saccades (**a**) Mean responses to rightward horizontal binocular optic flow moving in different speeds for Right HS (magenta) and right DNp15 (olive). The speed of the stimuli presented in the other panels of this figure, and of the rest of the figures in this study is highlighted in red. Gray shaded area indicates the duration of visual stimulation. Each trace corresponds to the grand mean of z-scored calcium responses. The mean response to 5-10 repetitions per stimulus from a single region of interest (ROI) at the axon terminals per fly was used to compute the garnd mean. Shaded area represents standard error of the mean. (**b**) Speed tuning curves calculated as the area under the curve during stimulus motion, normalized by the maximum response per ROI. (**c**) Responses of HS and DNP15 cells to differ- ent binocular and monocular optic flow stimuli. (**d**) Top, schematic illustrating directions of body translations and the resulting optic flow without rotating the head. Bottom, right HS (magenta) and DNp15 (olive) responses to translational optic flow. (**e**) Discrimination index for HS and DNp15 between different patterns of optic flow. Each circle represents an individual ROI. Colored horizontal line and black vertical line represents mean and 95% CI. (HS: N=12 flies, n=16 ROIs, DNp15: N=6 flies n=7 ROIs, *P < 0.05; **P < 0.01 ***P < 0.001, Wilcoxon's rank-sum test). (**f**) Immunostainings showing the stochastic expression of kir2.1:GFP in both, none, left or right DNp15 cells. (**g**) Effect of the stochastic silencing on saccade bias (see **Methods**). Number of flies per condition, none n=25; both n=31; left n=22; right n=22. The size of circles indicates the number of walking bouts per fly.

1146 **Figure 1-S2. LPTC axon terminals send outputs to and receive inputs from central**
1147 **neurons** (**a**) Left, schematic of the data coverage of the fly brain (dark gray) available from
1148 two large-scale fly brains imaged under EM resolution, FAFB and Flywire (top) and Hemibrain
1149 (bottom). Right, reconstructions of the right HSE cell in the three EM datasets. FAFB contains
1150 skeletonized neurons while FlyWire and Hemibrain provide volumetric recon- structions of
1151 cells. Postsynaptic (input) and presynaptic (output) site locations are marked with cyan and
1152 red dots, respectively. (**b**) Example EM section at the axon terminals of HSE (yellow) and a
1153 recurrent synaptic partner (green). Arrowheads indicate the location of presynaptic active
1154 zones. Scale bar, 1 μm. (**c**) Top, number of inputs (i.e. upstream partners) for H2, HS and VS
1155 cell classes in the posterior slope region of the fly central brain. Numbers in parentheses
1156 indicate number of cells present in each cell class. Presynaptic neurons traced for
1157 identification are colored based on the EM dataset. Synapses from untraced neurons are
1158 colored in gray. Bottom, same as Top, but for outputs (i.e., downstream partners). (**d**) Top,
1159 distribution of the number of synaptic connections between LPTCs and their inputs. Color-
1160 code indicates EM dataset and tracing status. Each distribution is normalized by total number
1161 of synapses. Inset shows a zoomed version of the region outlined by the dashed rectangle.
1162 Neurons with more than 10 synapses (black line) are considered strong inputs. Bottom, same
1163 as top, but for LPTC outputs. Neurons with more than 35 synapses (black line) are considered
1164 strong outputs.

1165 **Figure 1-S3: LPTCs have few strong, and many weak synaptic partners.** (**a**) Number of
1166 inputs H2 (top), HS (middle), and VS (bottom) cells receive from central neurons. Presynaptic
1167 central neurons are ordered from strongest to weakest. Color code indicates EM data- set.
1168 Inset, input numbers normalized by the strongest input cell (**b**) same as, **a**), but for LPTC
1169 outputs. (**c**) Pairwise matching of the strongest H2, HS (n=3) and VS (n=8) outputs across EM
1170 datasets. Cells are ordered based on total number of inputs they receive from each LPTC

1171 class. Matching is primarily based on a cell's anatomy, aided by its synaptic connectivity. Black
1172 lines represent matches where both pairs are within the top 10 strongest outputs in their
1173 respective EM dataset. Gray lines indicate that only one of the pairs is within the top 10.
1174 Dashed lines indicate uncertain matching due to the incomplete or bad segmentation in
1175 Hemibrain. See **Supplementary Table 1** for the cell identities.

1176 **Figure 2-S1: The synnaptic connectivity matrix among LPTC and their partners is**
1177 **structured.** The synnaptic connectivity matrix of HS, VS, H2 cells and their strongest synaptic
1178 partners in the central brain. Neurons are colored based on anatomical similarities, colorcode
1179 as in **Fig. 2** (see **Supplementary Table 2** for the complete list of neurons and nomenclature).
1180 The number of synaptic connections between pairs is indicated by the grayscale color code.
1181 In addition, connections are either colored red or blue based on the hierarchical clus- tering
1182 analysis, which represent whether connections belong to the H2-HS or VS networks,
1183 respectively (dendrogram, see **Methods**).

1184 **Figure 2-S2: The structure of the connectivity matrix is largely unaffected by synaptic**
1185 **thresholds.** The pairwise synaptic connectivity matrix among HS, VS, H2 cells their synaptic
1186 partners in the central brain, without applying any thresholds to the connectivity strength (232
1187 neurons total). Like in **Figure 2-S1**, number of synaptic connections between pairs is indicated
1188 by the grayscale color code. The dendrogram shows the hierarchical clustering analysis of
1189 the connectivity matrix (see **Methods**). Colored lines in the dendrogram indicate the cluster
1190 which the neuron belongs to in **Figure 2-S1**. The location of HS, H2 and VS cells within the
1191 matrix is highlighted.

1192 **Figure 2-S3: The middle layers of the H2-HS and VS networks are characterized by**
1193 **distinct classes of interneurons.** (**a**) Percentage of total number of inputs to the left H2 (left),
1194 right HS (middle) and right VS cells (right) grouped by class (color code). LPTC inputs that do

1195 not belong to the five major interneuron classes are grouped together as “other”. (**b**) Posterior
1196 view of the morphology of single cell examples from each LPTC input interneuron class. Red
1197 and cyan dots mark the location of pre- and postsynaptic sites, respectively. Regions of
1198 innervation are outlined in gray. (**c**) Anatomical reconstructions of bilateral populations of
1199 neurons per class. Top, posterior views; bottom, dorsal views. Each neural class forms a
1200 bilateral, mirror symmetric population (**d**) NBLAST-based anatomical clustering of the main
1201 backbones of the LPTC input interneurons. (**e**) Left, schematic of the fly brain with key
1202 neuropils sending projections to LPTC inputs. Right, percentage of total synaptic inputs of
1203 bLPTCrn (right) and cLPTCrn (right) cells in FlyWire grouped by the main brain regions where
1204 they receive dendritic input. (**f**) Same as **e**) but for the right DNp15 from FAFB. Input neurons
1205 from H2-HS network shown in **Figure 3a** are highlighted with colored lines. IPS - inferior
1206 posterior slope; SPS - superior posterior slope; GNG - gnathal ganglion; LOP - lobula plate;
1207 ME - medulla; VNC - ventral nerve cord.

1208 **Figure 3-S1: Transgenic lines used to gain access to H2-HS network neurons. (a)**
1209 Maximum intensity projections of transgenic lines labeling H2-HS network neurons. The
1210 specific cell class is indicated above each image (see **Methods** for a list of the transgenic
1211 lines). Neuropil (nc82) staining is shown in magenta, membrane targeted GFP or cytoplasmic
1212 GCaMP expression is shown in green. (**b**) Single-cell labeling using Multicolor FlpOut (MCFO)
1213 shows that the LPTCrn-Split Gal4 line contains both cLPTCrn (top) and uLPTCrn (bottom)
1214 cells. (**c**) Maximum intensity projections of transgenic lines that are heterozygous (left) or
1215 homozygous (right) mutants for *Rdl* in bIPS neurons. Neuropil staining is shown in magenta,
1216 cytoplasmic GCaMP expression is shown in green, TdToma- to expression, resulting from a
1217 successfully disruption of the Rdl gene with the FLP-Stop cassette, is shown in red. Note that
1218 one copy of Rdl-FlpStop gene is enough to express TdTomato in bIPS. Scale bar for all
1219 panels: 100 μm.

1220 **Figure 3-S2: Responses of H2-HS network neurons to different optic flow patterns.** (**a**)
1221 Top, schematics illustrating rotations of the fly's body along six degrees of freedom. Bottom,
1222 calci- um responses to the corresponding visual consequences of the body rotations from the
1223 fly's perspective in right HS (magenta), left H2 (blue), right bIPS (green), right H2rn (red) and
1224 right uLPTCrn (orange) cells. Gray shaded area shows the window of stimulation. Each trace
1225 corresponds to the grand mean± SEM (shade) of z-scored calcium responses obtained across
1226 flies. In each fly, mean responses were obtained from 5-10 repetitions of per stimulus from a
1227 single ROI at the axon terminals of the cells. (**b**) Left, responses of right HS, left H2, right
1228 bIPS, right H2rn and right uLPTCrn to horizontal optic flow moving CW at the indicated
1229 speeds. The speed of the rotational and translational optic flow presented in other figures is
1230 highlighted in red. Calcium responses are plotted the same way as in **a**). Right, speed tuning
1231 curves for each cell type. (**c**) Same as **a**), but for monocular stimuli. (**d**) Same as **a**), but for
1232 binocular symmetric optic flow. For all panels: HS: N=12 flies n=16 ROIs, H2: N =8 flies n=11
1233 ROIs, bIPS: N=15 flies n=16 ROIs, H2rn: N=5 flies n=8 ROIs, uLPTCrn: N=5 flies n=5 ROIs.

1234 **Figure 3-S3: Responses of H2-HS network neurons to translational optic flow** (**a**)
1235 Schematic illustrating possible body traveling directions (translations) and the corresponding
1236 optic flow without rotations of the head or body. (**b-f**) Calcium responses of right HS (**b**), left
1237 H2 (**c**), right bIPS (**d**), right H2rn (**e**) and right uLPTCrn (**f**) to translational optic flow patterns
1238 arranged in the same order as in **a**). Gray shaded area depicts the stimulation window. Each
1239 trace corresponds to the grand mean ± SEM (shaded area) of z-scored calcium responses
1240 obtained across flies. For each fly, mean responses to 5-10 repetitions per stimulus were
1241 obtained from a single ROI at the axon terminals. (**g**) Progressive-Sideslip discrimination index
1242 of neurons shown in panels **b-f**) (see **Methods**). Each circle represents an individual ROI.
1243 Colored horizontal line and black vertical line represents mean and 95% CI. (**h**) Same as **g**),
1244 but for Diagonal Translation vs. Sideslip discrimination index. For all panels: HS: N=10 flies

1245 n=10 ROIs, H2: N =8 flies n=9 ROIs, bIPS: N=9 flies n=9 ROIs, H2rn: N=5 flies n=8 ROIs,
1246 uLPTCrn: N=8 flies n=10 ROIs, *p < 0.05; **p < 0.01 ***p < 0.001, Wilcoxon's rank-sum test
1247 with Bonferroni correction for multiple comparisons).

1248 **Figure 4-S1: Central LPTC input neurons are GABAergic** (**a**) Representative confocal
1249 images showing immunoreactivity against GABA and GFP in cell bodies of each class of
1250 LPTC input neuron, as indicated on top of the images. Dashed circles outline cell bodies.
1251 Scale bar is 100 μm for full brain images and 10 μm for insets. (**b**) Reconstitution of the
1252 expression of each class of LPTCinput neurons by genetic intersection between LPTC input
1253 hemidrivers (columns) and GAD1 (top), ChaT (middle), or Vglut hemidrivers (bottom).
1254 Membrane-targeted GFP expression is shown in green, neuropil (nc82) staining is shown in
1255 magenta. Scale bar is 50 μm. Note the strong expression of each cell type under GAD1
1256 hemidriver and weak to no expression under ChaT and VGlut hemidrivers. A complete list of
1257 the genotypes can be found in **Supplementary Table 3**.

1258 **Figure 4-S2: bIPS synaptic inputs are organized non-randomly.** (**a**) Example of inputs to
1259 bIPS and the root point of the neuron. (**b**) Geodesic distance between bIPS root point and
1260 synaptic inputs from H2rn (n=192), HS (n=380), H2 (n=164), uLPTCrn (n=238), or a random
1261 subsample of the remaining inputs (n=192, see **Methods**). (**c**) Cumulative distribu- tions from
1262 (**b**). (**d**) Distance between an HS, H2 or other input synapse to bIPS and the clos- est H2rn
1263 input to bIPS. (**e-h**) Proportion of connectivity motifs that involve H2 (**e,g**) or HS (**f,h**) that
1264 converge onto bIPS (**e-f**) or DNp15 (**g-h**) with an additional neuron (cell X) color coded by cell
1265 type. Schematics at the top of each panel show the three cells involved. Numbered
1266 schematics show the connectivity motif plotted per graph.

1267 **Figure 5-S1: Calibration and parameters of the visually guided agent.** (**a**) Visual
1268 responses of simulated and real HS and H2 cells for different preferred (PD), non-preferred

1269 (NPD) and contralateral (Con) weights. (**b**) Visual responses of simulated and real bIPS and
1270 uLPTCIN cells for different HS, H2 and cross-connection weights. (**c**) Final table with manually
1271 adjusted weights based on visual responses from **a**) and **b**). (**d**) Schematic of the state flow
1272 of the modeled agent, and the associated distributions for saccades (inset, top) and activity
1273 bout size (inset, bottom) estimated from the real data. (**e**) Definition of the quality parameters,
1274 straightness, path deviation and angular bias. (**f**) Simulated straightness under dark
1275 conditions, as a function of 1/f noise level. Black line represents the mean straightness
1276 observed in real flies. (**g**) Simulated straight- ness under light conditions with visual feedback,
1277 as a function of visual weight. Black line represents the mean straightness observed in real
1278 flies. (**h**) Simulated straightness under dark (black) and light (gold) conditions for the chosen
1279 noise and visual weights. Shaded areas represent the standard error of straightness observed
1280 in real flies under light and dark conditions (Cruz et al. 2021)[38]

1281 **Figure 6-S1: Transgenic lines used in behavioral experiments** (**a**) Posterior view of
1282 maximal projection stacks of three different Split-Gal4 lines labeling bIPS. Neuropil (nc82)
1283 staining is shown in magenta and membrane targeted GFP expression is shown in green.
1284 Scale bar, 200 μm. (**b**) Posterior view of maximal stack projection of example brains with
1285 stochastic silencing of bIPS. Neuropil (nc82) staining is shown in magenta and membrane-
1286 targeted, Kir2.1-bound GFP expression is shown in green. Scale bar, 100 μm. For the
1287 complete list of genotypes of all transgenic lines, please see **Supplementary Table 3**.

1288 **Supplementary video 1: Optic flow stimuli used in this study.** Patterns of optic
1289 flow used in this study. Note that the LED arena is curved such that the middle of the
1290 video screen is in front of the fly while the edges are on either side of the fly (**Fig. 1c**).

1291 **Supplementary video 2: Speed tuning stimuli used in this study.** Example of
1292 binocular horizontal rotational optic flow presented at different speeds.

1293 ## References

1294 1. Mahajan, N. R. & Mysore, S. P. Donut-like organization of inhibition underlies
1295 categorical neural responses in the midbrain. *Nat. Commun. 2022 131* **13**, 1–
1296 17 (2022).

1297 2. Hu, Y. *et al.* A Neural Basis for Categorizing Sensory Stimuli to Enhance
1298 Decision Accuracy. *Curr. Biol.* **30**, 4896-4909.e6 (2020).

1299 3. Koyama, M. & Pujala, A. Mutual inhibition of lateral inhibition: a network motif
1300 for an elementary computation in the brain. *Curr. Opin. Neurobiol.* **49**, 69–74
1301 (2018).

1302 4. Tihana Jovanic, A. *et al.* Competitive Disinhibition Mediates Behavioral Choice
1303 and Sequences in Drosophila Article Competitive Disinhibition Mediates
1304 Behavioral Choice and Sequences in Drosophila. *Cell* **167**, 858–870 (2016).

1305 5. Zhao, W. *et al.* A disinhibitory mechanism biases Drosophila innate light
1306 preference. *Nat. Commun. 2019 101* **10**, 1–11 (2019).

1307 6. Gibson, J. J. *The Perception of the Visual World. The Philosophical Review*
1308 **60**, (The Riverside Press, 1950).

1309 7. Koenderink, J. J. Optic flow. *Vision Res.* **26**, 161–179 (1986).

1310 8. Wurtz, R. H. Optic flow: A brain region devoted to optic flow analysis? *Curr.*
1311 *Biol.* **8**, 554–556 (1998).

1312 9. Zhang, Y., Huang, R., Nörenberg, W. & Arrenberg, A. B. A robust receptive
1313 field code for optic flow detection and decomposition during self-motion. *Curr.*
1314 *Biol.* **32**, 2505-2516.e8 (2022).

1315 10. Kohn, J. R., Heath, S. L. & Behnia, R. Eyes matched to the prize: The state of
1316 matched filters in insect visual circuits. *Front. Neural Circuits* **12**, 26 (2018).

1317 11. Franz, M. O. & Krapp, H. G. Wide-field, motion-sensitive neurons and matched
1318 filters for optic flow fields. *Biol. Cybern.* **83**, 185–197 (2000).

1319 12. Barnes, W. J. P., Horseman, B. G. & Macauley, M. W. S. The Detection and

Analysis of Optic Flow by Crabs: from Eye Movements to Electrophysiology. in *The Crustacean Nervous System* (ed. Wiese, K.) 468–485 (Springer, Berlin, Heidelberg, 2002). doi:10.1007/978-3-662-04843-6_35

13. Britten, K. H. Mechanisms of Self-Motion Perception. *https://doi.org/10.1146/annurev.neuro.29.051605.112953* **31**, 389–410 (2008).

14. Hausen, K. The Lobula-Complex of the Fly: Structure, Function and Significance in Visual Behaviour. in *Photoreception and Vision in Invertebrates* 523–559 (Springer, Boston, MA, 1984). doi:10.1007/978-1-4613-2743-1_15

15. Matsuda, K. & Kubo, F. Circuit Organization Underlying Optic Flow Processing in Zebrafish. *Front. Neural Circuits* **15**, 73 (2021).

16. Paulk, A. C., Phillips-Portillo, J., Dacks, A. M., Fellous, J. M. & Gronenberg, W. The processing of color, motion, and stimulus timing are anatomically segregated in the bumblebee brain. *J. Neurosci.* **28**, 6319–6332 (2008).

17. Rasmussen, R. N., Matsumoto, A., Arvin, S. & Yonehara, K. Binocular integration of retinal motion information underlies optic flow processing by the cortex. *Curr. Biol.* **31**, 1165-1174.e6 (2021).

18. Lappe, M. *et al.* Perception of self-motion from visual flow. *Trends Cogn. Sci.* **3**, 329–336 (1999).

19. Warren, J., Kay, B. A., Zosh, W. D., Duchon, A. P. & Sahuc, S. Optic flow is used to control human walking. *Nat. Neurosci. 2001 42* **4**, 213–216 (2001).

20. Warren, W. H., Morris, M. W. & Kalish, M. Perception of Translational Heading From Optical Flow. *J. Exp. Psychol. Hum. Percept. Perform.* **14**, 646–660 (1988).

21. Angelaki, D. E. & Hess, B. J. M. Self-motion-induced eye movements: Effects on visual acuity and navigation. *Nat. Rev. Neurosci.* **6**, 966–976 (2005).

22. Cullen, K. E. & Taube, J. S. Our sense of direction: Progress, controversies and challenges. *Nat. Neurosci.* **20**, 1465–1473 (2017).

1347 23. Theobald, J. Insect Flight: Navigating with Smooth Turns and Quick Saccades.
1348 *Curr. Biol.* **27**, R1125–R1127 (2017).

1349 24. Kim, A. J., Fitzgerald, J. K. & Maimon, G. Cellular evidence for efference copy
1350 in Drosophila visuomotor processing. *Nat. Neurosci.* **18**, 1247–1255 (2015).

1351 25. Fenk, L. M., Kim, A. J. & Maimon, G. Suppression of motion vision during
1352 course-changing, but not course-stabilizing, navigational turns. *Curr. Biol.* **31**,
1353 4608-4619.e3 (2021).

1354 26. Duffy, C. J. MST neurons respond to optic how and translational movement. *J.*
1355 *Neurophysiol.* **80**, 1816–1827 (1998).

1356 27. Fujiwara, T., Cruz, T. L., Bohnslav, J. P. & Chiappe, M. E. A faithful internal
1357 representation of walking movements in the Drosophila visual system. *Nat.*
1358 *Neurosci.* **20**, 72–81 (2017).

1359 28. Borst, A., Haag, J. & Reiff, D. F. Fly motion vision. *Annu. Rev. Neurosci.* **33**,
1360 49–70 (2010).

1361 29. Farrow, K., Haag, J. & Borst, A. Nonlinear, binocular interactions underlying
1362 flow field selectivity of a motion-sensitive neuron. *Nat. Neurosci.* **9**, 1312–1320
1363 (2006).

1364 30. Pokusaeva, V. O., Satapathy, R., Symonova, O. & Jösch, M. Gap junctions
1365 arbitrate binocular course control in flies. *bioRxiv* 2023.05.31.543181 (2023).
1366 doi:10.1101/2023.05.31.543181

1367 31. Haag, J. & Borst, A. Orientation tuning of motion-sensitive neurons shaped by
1368 vertical-horizontal network interactions. *J. Comp. Physiol. A Neuroethol.*
1369 *Sensory, Neural, Behav. Physiol.* **189**, 363–370 (2003).

1370 32. Schnell, B. *et al.* Processing of horizontal optic flow in three visual
1371 interneurons of the Drosophila brain. *J. Neurophysiol.* **103**, 1646–1657 (2010).

1372 33. Cruz, T. *et al.* Motor context coordinates visually guided walking in Drosophila.
1373 *bioRxiv* 1–49 (2019). doi:10.1101/572792

34. Zhao, A. *et al.* Eye structure shapes neuron function in Drosophila motion vision. *bioRxiv* 2022.12.14.520178 (2022).

35. Busch, C., Borst, A. & Mauss, A. S. Bi-directional Control of Walking Behavior by Horizontal Optic Flow Sensors. *Curr. Biol.* **28**, 4037-4045.e5 (2018).

36. Fujiwara, T., Brotas, M. & Chiappe, M. E. Walking strides direct rapid and flexible recruitment of visual circuits for course control in Drosophila. *Neuron* **110**, 2124-2138.e8 (2022).

37. Suver, M. P., Huda, A., Iwasaki, N., Safarik, S. & Dickinson, M. H. An array of descending visual interneurons encoding self-motion in Drosophila. *J. Neurosci.* **36**, 11768–11780 (2016).

38. Cruz, T. L., Pérez, S. M. & Chiappe, M. E. Fast tuning of posture control by visual feedback underlies gaze stabilization in walking Drosophila. *Curr. Biol.* **31**, 4596–4607 (2021).

39. Namiki, S., Dickinson, M. H., Wong, A. M., Korff, W. & Card, G. M. The functional organization of descending sensory-motor pathways in drosophila. *Elife* **7**, (2018).

40. Zheng, Z. *et al.* A Complete Electron Microscopy Volume of the Brain of Adult Drosophila melanogaster. *Cell* **174**, 730-743.e22 (2018).

41. Dorkenwald, S. *et al.* FlyWire: Online community for whole-brain connectomics. *bioRxiv* 2020.08.30.274225 (2020). doi:10.1101/2020.08.30.274225

42. Scheffer, L. K. *et al.* A connectome and analysis of the adult drosophila central brain. *Elife* **9**, 1–74 (2020).

43. Hengstenberg, R. Gaze control in the blowfly Calliphora: a multisensory, two-stage integration process. *Semin. Neurosci.* **3**, 19–29 (1991).

44. Parsons, M. M., Krapp, H. G. & Laughlin, S. B. A motion-sensitive neurone responds to signals from the two visual systems of the blowfly, the compound eyes and ocelli. *J. Exp. Biol.* **209**, 4464–4474 (2006).

1402 45. Eckert, H. & Dvorak, D. R. The centrifugal horizontal cells in the lobula plate of
1403 the blowfly, Phaenicia sericata. *J. Insect Physiol.* **29**, 547–560 (1983).

1404 46. Wei, H., Kyung, H. Y., Kim, P. J. & Desplan, C. The diversity of lobula plate
1405 tangential cells (LPTCs) in the Drosophila motion vision system. *J. Comp.*
1406 *Physiol. A Neuroethol. Sensory, Neural, Behav. Physiol.* **206**, 139–148 (2020).

1407 47. Rayshubskiy, A. *et al.* Neural control of steering in walking Drosophila. *bioRxiv*
1408 2020.04.04.024703 (2020).

1409 48. Namiki, S. & Kanzaki, R. Brain Premotor Centers for Pheromone Orientation
1410 Behavior. 243–264 (2020). doi:10.1007/978-981-15-3082-1_12

1411 49. Namiki, S., Wada, S. & Kanzaki, R. Descending neurons from the lateral
1412 accessory lobe and posterior slope in the brain of the silkmoth Bombyx mori.
1413 *Sci. Reports 2018 81* **8**, 1–19 (2018).

1414 50. Kim, A. J., Fenk, L. M., Lyu, C. & Maimon, G. Quantitative Predictions
1415 Orchestrate Visual Signaling in Drosophila. *Cell* **168**, 280-294.e12 (2017).

1416 51. Fischer, P. J. & Schnell, B. Multiple mechanisms mediate the suppression of
1417 motion vision during escape maneuvers in flying Drosophila. *iScience* **25**,
1418 105143 (2022).

1419 52. Eckstein, N. *et al.* Neurotransmitter classification from electron microscopy
1420 images at synaptic sites in Drosophila. *bioRxiv* (2020).
1421 doi:10.1101/2020.06.12.148775

1422 53. Fisher, Y. E. *et al.* FlpStop, a tool for conditional gene control in Drosophila.
1423 *Elife* **6**, (2017).

1424 54. Ffrench-Constant, R. H., Roush, R. T., Mortlock, D. & Dively, G. P. Isolation of
1425 Dieldrin Resistance from Field Populations of Drosophila melanogaster
1426 (Diptera: Drosophilidae). *J. Econ. Entomol.* **83**, 1733–1737 (1990).

1427 55. Ffrench-Constant, R. H., Rocheleau, T. A., Steichen, J. C. & Chalmers, A. E. A
1428 point mutation in a Drosophila GABA receptor confers insecticide resistance.
1429 *Nat. 1993 3636428* **363**, 449–451 (1993).

1430 56. Hosie, A. M., Aronstein, K., Sattelle, D. B. & Ffrench-Constant, R. H. Molecular
1431 biology of insect neuronal GABA receptors. *Trends Neurosci.* **20**, 578–583
1432 (1997).

1433 57. Haag, J., Wertz, A. & Borst, A. Central gating of fly optomotor response. *Proc.*
1434 *Natl. Acad. Sci. U. S. A.* **107**, 20104–20109 (2010).

1435 58. Wertz, A., Haag, J. & Borst, A. Local and global motion preferences in
1436 descending neurons of the fly. *J. Comp. Physiol. A. Neuroethol. Sens. Neural.*
1437 *Behav. Physiol.* **195**, 1107–1120 (2009).

1438 59. Wertz, A., Haag, J. & Borst, A. Integration of binocular optic flow in cervical
1439 neck motor neurons of the fly. *J. Comp. Physiol. A Neuroethol. Sensory,*
1440 *Neural, Behav. Physiol.* **198**, 655–668 (2012).

1441 60. Strausfeld, N. J., Seyan, H. S. & Milde, J. J. The neck motor system of the fly
1442 Calliphora erythrocephala - I. Muscles and motor neurons. *J. Comp. Physiol. A*
1443 **160**, 205–224 (1987).

1444 61. Huston, S. J. & Krapp, H. G. Visuomotor Transformation in the Fly Gaze
1445 Stabilization System. *PLOS Biol.* **6**, e173 (2008).

1446 62. Haag, J., Wertz, A. & Borst, A. Integration of Lobula Plate Output Signals by
1447 DNOVS1, an Identified Premotor Descending Neuron. *J. Neurosci.* **27**, 1992–
1448 2000 (2007).

1449 63. Strausfeld, N. J. & Bassemir, U. K. Lobula plate and ocellar interneurons
1450 converge onto a cluster of descending neurons leading to neck and leg motor
1451 neuropil in Calliphora erythrocephala. *Cell Tissue Res.* **240**, 617–640 (1985).

1452 64. Kress, D. & Egelhaaf, M. Head and body stabilization in blowflies walking on
1453 differently structured substrates. *J. Exp. Biol.* **215**, 1523–1532 (2012).

1454 65. Schilstra, C. & Van Hateren, J. H. Stabilizing gaze in flying blowflies. *Nat. 1998*
1455 *3956703* **395**, 654–654 (1998).

1456 66. Seelig, J. D. & Jayaraman, V. Neural dynamics for landmark orientation and
1457 angular path integration. *Nat. 2015 5217551* **521**, 186–191 (2015).

1458 67. Green, J. *et al.* A neural circuit architecture for angular integration in
1459 Drosophila. *Nat. 2017 5467656* **546**, 101–106 (2017).

1460 68. Turner-Evans, D. B. *et al.* The Neuroanatomical Ultrastructure and Function of
1461 a Biological Ring Attractor. *Neuron* **108**, 145-163.e10 (2020).

1462 69. Fisher, Y. E., Marquis, M., D'Alessandro, I. & Wilson, R. I. Dopamine promotes
1463 head direction plasticity during orienting movements. *Nat. 2022 6127939* **612**,
1464 316–322 (2022).

1465 70. Mauss, A. S. *et al.* Neural Circuit to Integrate Opposing Motions in the Visual
1466 Field. *Cell* **162**, 351–362 (2015).

1467 71. Braun, A., Borst, A. & Meier, M. Disynaptic inhibition shapes tuning of OFF-
1468 motion detectors in Drosophila. *Curr. Biol.* **33**, 2260-2269.e4 (2023).

1469 72. Kress, D. & Egelhaaf, M. Gaze characteristics of freely walking blowflies
1470 Calliphora vicina in a goal-directed task. *J. Exp. Biol.* **217**, 3209–3220 (2014).

1471 73. Koyama, M. *et al.* A circuit motif in the zebrafish hindbrain for a two alternative
1472 behavioral choice to turn left or right. *Elife* **5**, (2016).

1473 74. Essig, J., Hunt, J. B. & Felsen, G. Inhibitory neurons in the superior colliculus
1474 mediate selection of spatially-directed movements. *Commun. Biol. 2021 41* **4**,
1475 1–14 (2021).

1476 75. Haag, J. & Borst, A. Recurrent network interactions underlying flow-field
1477 selectivity of visual interneurons. *J. Neurosci.* **21**, 5685–5692 (2001).

1478 76. Silies, M., Gohl, D. M. & Clandinin, T. R. Motion-Detecting Circuits in Flies:
1479 Coming into View. (2014). doi:10.1146/annurev-neuro-071013-013931

1480 77. Borst, A. & Helmstaedter, M. Common circuit design in fly and mammalian
1481 motion vision. *Nat. Neurosci.* **18**, 1067–1076 (2015).

1482 78. Agrochao, M., Tanaka, R., Salazar-Gatzimas, E. & Clark, D. A. Mechanism for
1483 analogous illusory motion perception in flies and humans. *Proc. Natl. Acad.*
1484 *Sci. U. S. A.* **117**, 23044–23053 (2020).

1485 79. Nern, A., Pfeiffer, B. D. & Rubin, G. M. Optimized tools for multicolor
1486 stochastic labeling reveal diverse stereotyped cell arrangements in the fly
1487 visual system. *Proc. Natl. Acad. Sci. U. S. A.* **112**, E2967–E2976 (2015).

1488 80. Lyu, C., Abbott, L. F. & Maimon, G. Building an allocentric travelling direction
1489 signal via vector computation. *Nat. 2021 6017891* **601**, 92–97 (2021).

1490 81. Molina-Obando, S. *et al.* On selectivity in the drosophila visual system is a
1491 multisynaptic process involving both glutamatergic and GABAergic inhibition.
1492 *Elife* **8**, (2019).

1493 82. Asahina, K. *et al.* Tachykinin-expressing neurons control male-specific
1494 aggressive arousal in drosophila. *Cell* **156**, 221–235 (2014).

1495 83. Diao, F. *et al.* Plug-and-Play Genetic Access to Drosophila Cell Types using
1496 Exchangeable Exon Cassettes. *Cell Rep.* **10**, 1410–1421 (2015).

1497 84. Bates, A. S. *et al.* The natverse, a versatile toolbox for combining and
1498 analysing neuroanatomical data. *Elife* **9**, (2020).

1499 85. Schneider-Mizell, C. M. *et al.* Quantitative neuroanatomy for connectomics in
1500 Drosophila. *Elife* **5**, 1–36 (2016).

1501 86. Saalfeld, S., Cardona, A., Hartenstein, V. & Tomančák, P. CATMAID:
1502 Collaborative annotation toolkit for massive amounts of image data.
1503 *Bioinformatics* **25**, 1984–1986 (2009).

1504 87. Buhmann, J. *et al.* Automatic detection of synaptic partners in a whole-brain
1505 Drosophila electron microscopy data set. *Nat. Methods* **18**, 771–774 (2021).

1506 88. Bates, A. S. *et al.* Complete Connectomic Reconstruction of Olfactory
1507 Projection Neurons in the Fly Brain. *Curr. Biol.* **30**, 3183-3199.e6 (2020).

1508 89. Schlegel, P. *et al.* A consensus cell type atlas from multiple connectomes
1509 reveals principles of circuit stereotypy and variation. *bioRxiv*
1510 2023.06.27.546055 (2023). doi:10.1101/2023.06.27.546055

1511 90. Jenett, A. *et al.* A GAL4-Driver Line Resource for Drosophila Neurobiology.

1512 *Cell Rep.* **2**, 991–1001 (2012).

1513 91. Tirian, L. & Dickson, B. J. The VT GAL4, LexA, and split-GAL4 driver line
1514 collections for targeted expression in the Drosophila nervous system. *bioRxiv*
1515 198648 (2017). doi:10.1101/198648

1516 92. Meissner, G. W. *et al.* An image resource of subdivided Drosophila GAL4-
1517 driver expression patterns for neuron-level searches. *bioRxiv*
1518 2020.05.29.080473 (2020). doi:10.1101/2020.05.29.080473

1519 93. Otsuna, H., Ito, M. & Kawase, T. Color depth MIP mask search: a new tool to
1520 expedite Split-GAL4 creation. *bioRxiv* 318006 (2018). doi:10.1101/318006

1521 94. Dionne, H., Hibbard, K. L., Cavallaro, A., Kao, J. C. & Rubin, G. M. Genetic
1522 Reagents for Making Split-GAL4 Lines in Drosophila. *Genetics* **209**, 31–35
1523 (2018).

1524 95. Crickmore, M. A. & Vosshall, L. B. Opposing Dopaminergic and GABAergic
1525 Neurons Control the Duration and Persistence of Copulation in Drosophila.
1526 *Cell* **155**, 881–893 (2013).

1527 96. Reiser, M. B. & Dickinson, M. H. A modular display system for insect
1528 behavioral neuroscience. *J. Neurosci. Methods* **167**, 127–139 (2008).

1529 97. Weir, P. T. & Dickinson, M. H. Functional divisions for visual processing in the
1530 central brain of flying Drosophila. *Proc. Natl. Acad. Sci. U. S. A.* **112**, E5523–
1531 E5532 (2015).

1532 98. Dana, H. *et al.* High-performance calcium sensors for imaging activity in
1533 neuronal populations and microcompartments. *Nat. Methods* **16**, 649–657
1534 (2019).

1535 99. Chen, T. W. *et al.* Ultrasensitive fluorescent proteins for imaging neuronal
1536 activity. *Nat. 2013 4997458* **499**, 295–300 (2013).

1537 100. Thurman, S. T., Guizar-Sicairos, M. & Fienup, J. R. Efficient subpixel image
1538 registration algorithms. *Opt. Lett. Vol. 33, Issue 2, pp. 156-158* **33**, 156–158
1539 (2008).

1540 101. Eichner, H., Joesch, M., Schnell, B., Reiff, D. F. & Borst, A. Internal Structure
1541 of the Fly Elementary Motion Detector. *Neuron* **70**, 1155–1164 (2011).

1542 102. Costa, M., Manton, J. D., Ostrovsky, A. D., Prohaska, S. & Jefferis, G. S. X. E.
1543 NBLAST: Rapid, Sensitive Comparison of Neuronal Structure and
1544 Construction of Neuron Family Databases. *Neuron* **91**, 293–311 (2016).

1545 103. Hulse, B. K. *et al.* A connectome of the drosophila central complex reveals
1546 network motifs suitable for flexible navigation and context-dependent action
1547 selection. *Elife* **10**, (2021).

1548 104. Vanwalleghem, G., Constantin, L. & Scott, E. K. Calcium Imaging and the
1549 Curse of Negativity. *Front. Neural Circuits* **14**, 607391 (2021).

1550

1551

1552

Figure 1: DNp15 exhibit enhanced sensitivity to rotational optic flow compared to HS cells and plays a role in steering during high-speed translation

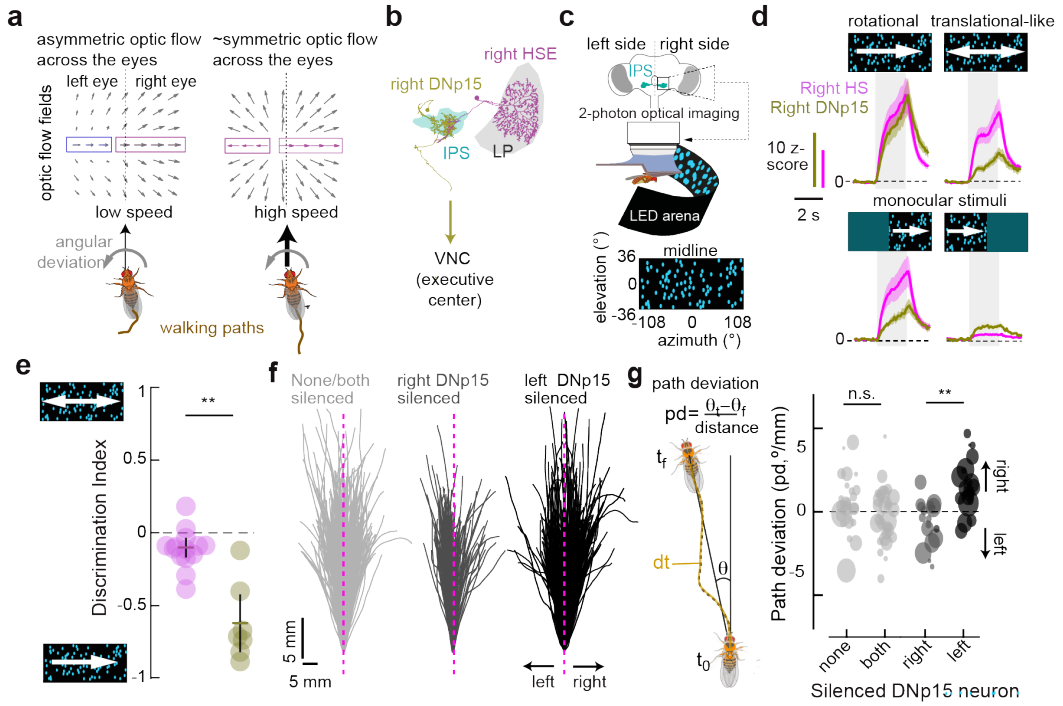

Figure 1: DNp15 exhibit enhanced sensitivity to rotational optic flow compared to HS and plays a role in steering during high-speed translation (**a**) Simulated binocular optic flow of a fly walking at low (left) versus high (right) forward speed and rotating with the same angular velocity. Rectangles indicate the presence of regressive (blue) or progressive (magenta) motion detected by a horizontal motion-sensitive system. (**b**) EM-reconstructed right HS (magenta) and postsynaptic right DNp15 (olive) cells. The chemical and electrical synapses between the two cells allocated within the inferior posterior slope (IPS, cyan), a premotor region. The dendrites of HS cells are located within the lobula plate (LP). (**c**) Top, schematic of the fly brain and the IPS, where optical imaging was performed. Bottom, 2-photon calcium imaging setup and the visual LED display. (**d**) HS (magenta) and DNp15 (olive) calcium responses to horizontal binocular rotational or translational-like optic flow (top), and to monocular optic flow (bottom). (**e**) Discrimination index (see **Methods**) between translational-like and rotational stimuli in HS (magenta) and DNp15 (olive). Each circle represents an individual ROI. Colored horizontal line and black vertical line represent the mean and 95% CI. (HS: N=12 flies, n=16 ROIs, DNp15: N=6 flies n=7 ROIs, *P < 0.05; **P < 0.01 ***P < 0.001, Wilcoxon's rank-sum test). (**f**) The walking paths of forward runs of length ≥ 4 body lengths, aligned at their origin, in flies with either both or none DNP15 silenced (left, light gray traces), right DNP15 silenced (middle, gray traces), and left DNP15 silenced (right, black traces). (**g**) Left, definition of path deviation, the difference in body orientation between the end and the beginning of the walking path over traveled distance. Right, mean path deviation from per fly in flies with none, single or both DNp15 silenced. The size of the circle indicates the number of walking bouts per fly, with larger sizes representing larger number of walking bouts. Number of flies per condition, none n=25; both n=31; left n=22; right n=22; $*p < 0.05$ $**p < 0.01$ $***p < 0.001$, Wilcoxon's rank-sum test with Bonferroni correction for multiple comparisons.)

1553

Figure 2: H2, HS and VS cells form two distinctive networks in the central brain

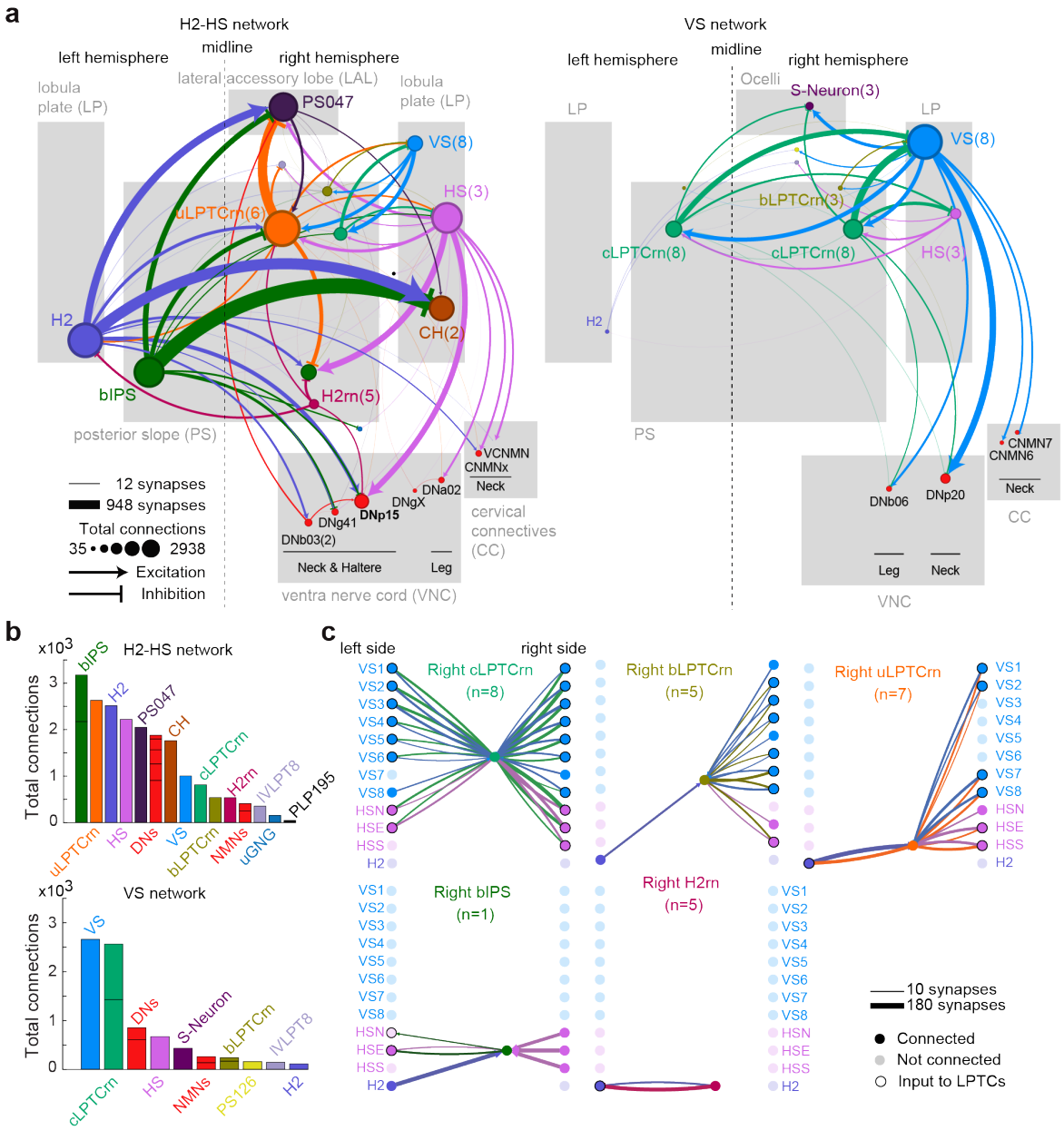

Figure 2. H2, HS and VS cells form two distinctive networks in the central brain. (**a**) Connectivity graph of the H2-HS (left) and VS (right) networks. Neurons are represented as nodes (circles), with their synaptic connections indicated by arrows (predicted to be excitatory) or circled edges (predicted to be inhibitory). Thickness of the arrows/circled edges represents number of synapses, and color indicates the presynaptic neuron. For clarity, connections with fewer than 10 synapses are not shown; connections with fewer than 50 synapses are shaded. Node diameters represent the total number of connections that each node has within the network (including both inputs and outputs). Except for LPTCs, nodes are placed within the brain regions (grey rectangles) where their axons reside. (**b**) The total number of synaptic connections for each neuron within H2-HS network (Top), and VS network (bottom). See **Supplementary Table 2** for the complete list of neurons and nomenclature. (**c**) Connectivity graph between each LPTC input cell type and individual HS, H2 and VS cells. Edges indicate synaptic connection between cells, with thickness indicating number of synapses and color indicating the presynaptic cell. LPTCs without input are transparent for clarity.

Figure 3: Binocular interactions in optic flow sensitivity within the H2-HS network

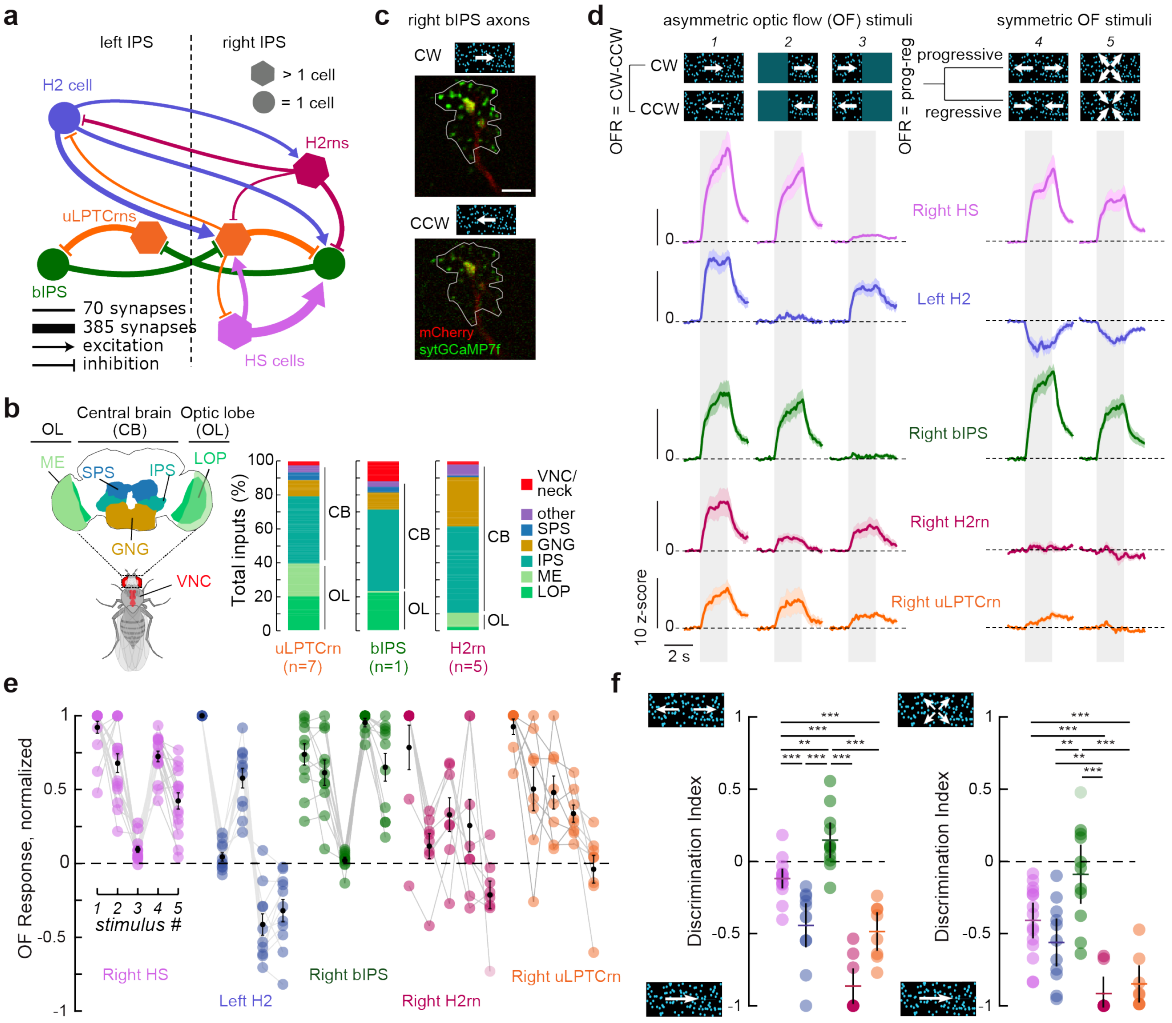

Figure 3: Binocular interactions define optic flow sensitivity in H2-HS interneurons. (**a**) Local connectivity between the input and middle layers of the H2-HS network. (**b**) Left, schematic of the central nervous system (CNS) regions from which uLPTCrns, bIPS and H2rns receive inputs. LOP, Lobula Plate; ME, Medulla; GNG, gnathal ganglia; IPS, inferior poste-rior slope; SPS, superior posterior slope. Right, proportion of inputs per CNS region (color code) for each interneuron. (**c**) Single plane fluorescence image of an example recording from bIPS axons during binocular CW (top) and CCW (bottom) horizontal motion. We efined a single region of interest (ROI), which covers the entire axon is outlined in white. The red signal corresponds to mCherry fluorescence, whereas the green signal corresponds to sytGCaMP7f fluorescence. Scale bar, 10 µm. (**d**) Top: visual stimuli presented to the fly, with direction of motion as indicated by arrows. Bottom: optic flow calcium responses (OFR) of each neuron to rotational (stimuli *1, 2, 3*) or translational (stimuli *4, 5*) optic flow. OFR for rotational stimuli is defined as CW (rightwards) minus CCW (leftwards) direction of visual motion. For the translational stimuli, OFR is defined as progressive minus regressive direction of visual motion. Each trace corresponds to the grand mean of the z-scored calcium response across flies ± SEM (shade). Per fly, we obtained mean responses to 5-10 repetitions per stimulus. Light-gray rectangles indicate the stimulation window. For this and the remaining panels: HS: N=12 flies n=16 ROIs, H2: N =8 flies n=11 ROIs, bIPS: N=10 flies n=11 ROIs, H2rn: N=5 flies n=8 ROIs, uLPTCrn: N=6 flies n=8 ROIs. (**e**) Normalized OFRs (relative to the preferred stimulus per neuron). Error bars represent SEM of the grand mean across flies. (**f**) Left, discrimination index between translation-like vs. rotational stimuli (see **Methods**). Each circle represents an individual ROI. The horizontal line and black vertical line represent mean and 95% CI. Right, discrimination index between translation vs. rotational stimuli. *: $p < 0.05$; **$p < 0.01$; ***$p < 0.001$, Wilcoxon's rank-sum test with Bonferroni correction for multiple comparisons.

Figure 4: GABAergic inhibition fine-tunes optic flow responses in bIPS

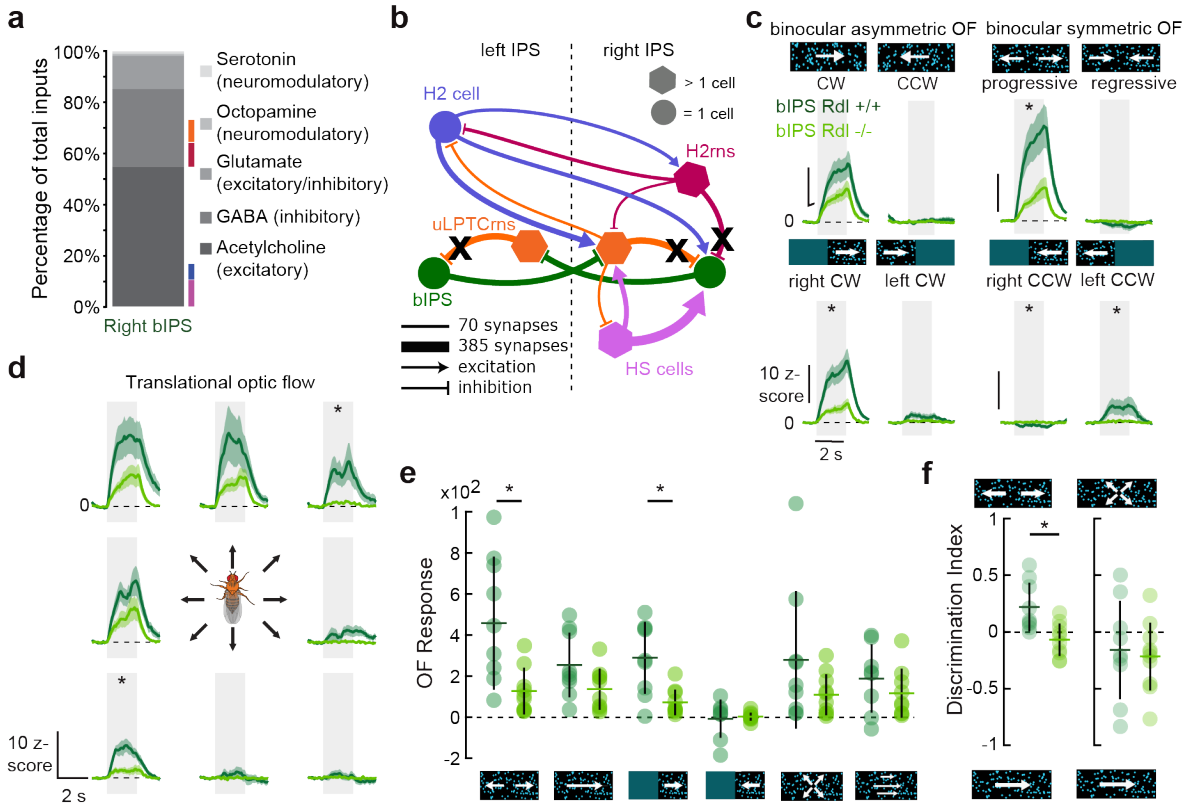

Figure 4: GABAergic inhibition fine-tunes optic flow responses in bIPS. (**a**) Right bIPS input profile, grouped by their predicted primary neurotransmitter. Neurons shown in **b**) are highlighted with colored lines. (**b**) Schematic of the local connectivity of the input and middle layers of the H2-HS network. Inhibitory connections are shown as tee shaped edges. Blocking Rdl receptors in bIPS using FLPStop disrupts fast GABAergic signaling onto bIPS (black crosses). (**c**) Neural responses of wild type (dark green) and Rdl-disrupted (light green) bIPS cells to binocular asymmetric (left, rotational) and symmetric (right, translational-like) optic flow (OF). Each trace corresponds to the grand mean ± SEM (shaded area) of z-scored calcium responses obtained across flies. For each fly, mean responses to 5-10 repetitions per stimulus were obtained from a single ROI at the axon terminals. Stimuli with a star indicate area under the curve (auc) responses that are statistically different from wild-type bIPS recordings. (**d**) Same as **c**), but for translational optic flow. (**e**) OF responses, the difference between the preferred and nulled direction responses (auc) for horizontal and progressive visual motion. (**f**) Left, discrimination index between translational-like and rotational optic flow of recorded neurons in **c**) (see **Methods**). Each circle represents an individual ROI. Colored horizontal line and black vertical line represents mean and 95% CI. Right, discrimination index between progressive and rotational optic flow. For all panels: bIPS: N=7 flies n=9 ROIs, bIPS Rdl-FLPStop: N=7 flies n=10 ROIs. *P < 0.05; **P < 0.01 ***P < 0.001, Wilcoxon's rank-sum test.

Figure 5: A lateral disinhibitory motif enhance asymmetries in neural activity across the right versus left hemisphere

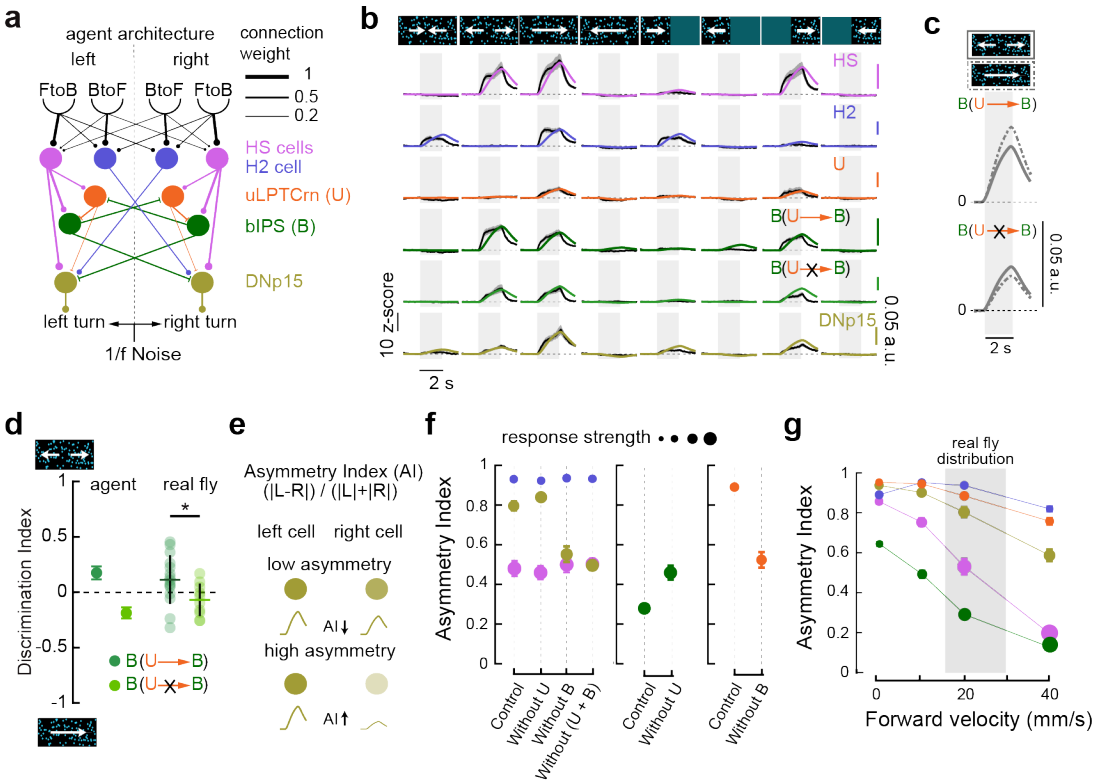

Figure 5: A lateral disinhibitory motif enhance asymmetries in neural activity across the right versus left hemisphere. (**a**) Schematic of the agent architecture: two sets of Reichardt detectors tuned to front-to-back (FtoB) or back-to-front (BtoF) motion detect the optic flow generated by a simulated walking fly (See **Methods**, **Fig. 5-S1**). The detected visual motion is processed by a network of nodes that mimic the core network motif of H2-HS network (**Fig. 3a**). The weights that connect the nodes are tuned based on a subset of measured visual responses (**Fig. 5-S1**). (**b**) Simulated and observed visual responses to monocular and binocular patterns of optic flow. Responses were matched to the maximal observed response. Observed responses are replotted from **Fig. 3-S2** and **Fig. 4c** (**c**) Visual response of modeled bIPS to symmetric or asymmetric binocular optic flow, and with or without a functional input from uLPTCrns. (**d**) Left: discrimination index of modeled and observed bIPS with or without a functional input from uLPTCrns. Right: observedd bIPS' discrimination index with or without functional GABAergic input (replotted from **Fig. 4f**). (**e**) Definition of the Asymmetry Index (AI) and two example conditions with low and high AI values. (**f**) Asymmetry index of simulated neurons (colored) in the full model (Control), under bIPS silencing (Without B), under uLPTCrn silencing (Without U) and under both bIPS and uLPTCrn silencing (With-out U+B). The dot size corresponds to the magnitude of the neural response. (**g**) Asymmetry index of simulated neurons (colored) in the full model varying the forward velocity of the agent. The shaded area corresponds to the range of velocities observed for forward runs in real exploratory flies (Cruz et al. 2021).

Figure 6: bIPS plays a role in steering control during highspeed walking

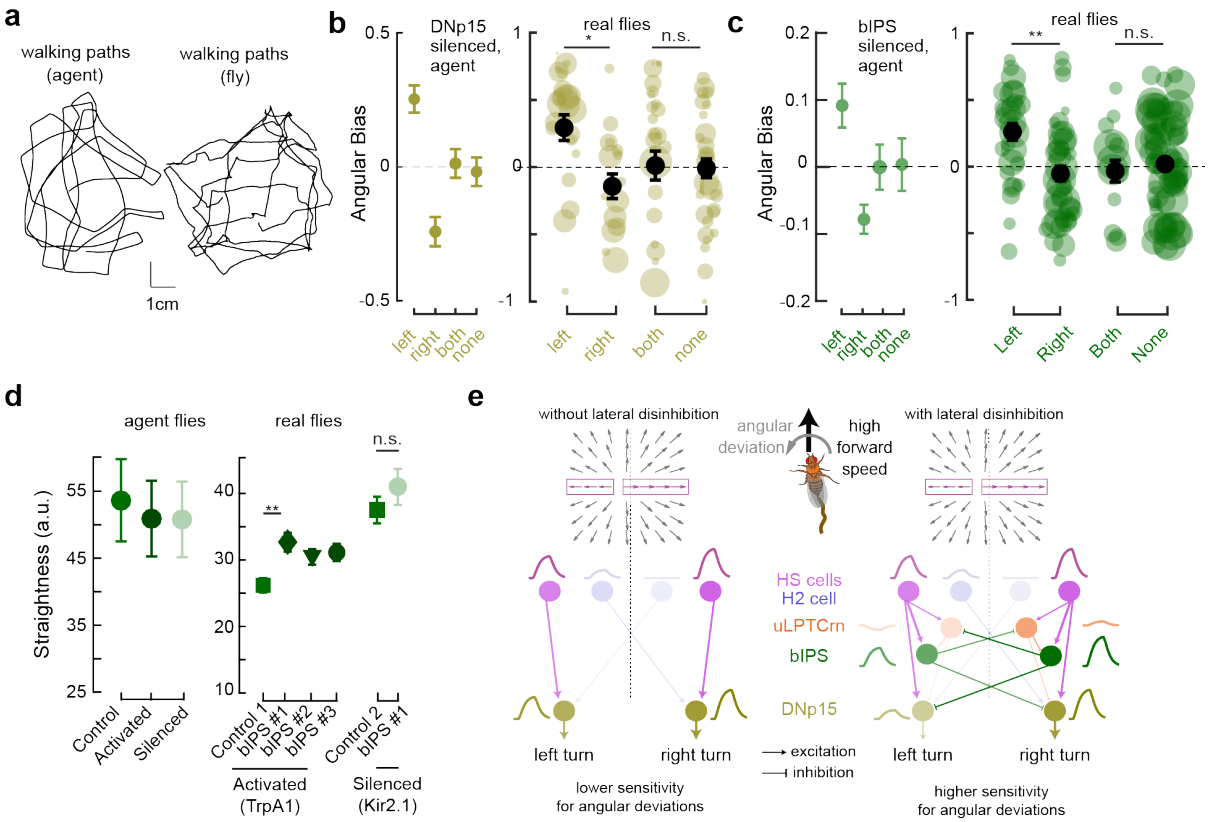

Figure 6: bIPS plays a role in steering control during highspeed walking. (**a**) Example walking paths of the agent (left) and the real fly (right) under prominent visual feedback. (**b**) Simulated (left) and real fly (right) angular bias during forward runs (see **Methods**) with DNp15 activity perturbed bilateral or unilaterally. Transparent dots depict mean bias of individual flies, black dots represent grand mean per genotype, weighted by the amount of walking bouts (dot size). Error bars represent SEM. Number of flies per condition, None n=25; Left n=22; Right n=22; Both n=31. (**c**) Same as **b**), but for bIPS. Number of flies per condition, None n=65; Left n=26; Right n=38; Both n=13. For (**b**) and (**c**): *p < 0.05; **p < 0.01 ***p < 0.001, Wilcoxon's rank-sum test with Bonferroni correction for multiple comparisons. (**d**) Left, simulated straightness of the agent during forward runs (see **Methods**) with control (green), bilaterally activated (dark green) or silenced (light green) bIPS cells. Right, straigtness of control flies (green), or flies with bilaterally activated (dark green) or silenced (light green) bIPS cells. Number of flies per condition, empty control>TrpA1 n=25; bIPS#1>TrpA1 n=27; bIPS#2>TrpA1 n=25; bIPS#3>Tr-pA1 n=29; empty control>Kir2.1 n=22; bIPS#1>Kir2.1 n=23. (**e**) Summary of the findings. The middle layer of the H2-HS network supports steering by enhancing the difference in the activity levels of the output layer across hemispheres. This function is driven by a competitive disinhibitory motif that is well posed to be recruited at highspeed walking. In this condition, binocular optic flow may contain prominent translational components, possibly overshadowing rotational cues that are critical for course control. We propose that the competitive disinhibition at the middle layer plays an important role in modulating the output layer in a continuous and dynamic manner, leading to a more robust estimate of the deviations from a straight course.

1562